Mémoire

Auteur : Mouton, Alyssa
Promoteur(s) : Bonfond, Bertrand
Faculté : Faculté des Sciences
Diplôme : Master en sciences spatiales, à finalité approfondie
Année académique : 2024-2025
URI/URL : http://hdl.handle.net/2268.2/23876

Université de Liège

Master's Thesis

Characterizing auroral arcs in Jupiter's outer emissions

Master in Space Sciences

Author :
Alyssa Mouton

Supervisor :
Bertrand Bonfond

Research Focus

Academic year 2024-2025

Abstract

Characterizing auroral arcs in Jupiter's outer emissions

This thesis presents a statistical study of auroral signatures associated with particle injections at Jupiter. Auroral injections are events where populations of energetic particles are rapidly accelerated and injected into Jupiter's magnetosphere. The signature of these injections manifest as compact auroral structures, reflecting localized increases in high-energy particle populations that move azimuthally around the planet, guided by magnetic field gradients and curvature. They can exhibit a longitudinal shift between the brightness peak and the color ratio peak. This shift is defined as negative when higher-energy particles begin their differential drift relative to lower-energy particles, producing an offset downstream in the direction of plasma rotation around the planet. In her thesis, Dumont (2023) reported a surprisingly high number of positive shifts that were difficult to explain physically; these results were likely influenced by limitations in the auroral image reconstruction technique. In this thesis, an improved map reconstruction method is developped, specifically designed to reduce such artifacts, providing a more accurate representation of particle injections and their associated shifts.

Using ultraviolet spectral data collected by the Ultraviolet Spectrograph (UVS) instrument aboard the Juno spacecraft, a comprehensive analysis was performed on 693 injection events to characterize the spatial and temporal relationships between auroral features. Auroral injections are mapped to Jupiter's equatorial plane using the JRM33 magnetic field model. For each event, intensity profiles of both brightness and color ratio are extracted along arcs crossing the injection coordinates. The intensities are measured on brightness and color ratio maps, reconstructed from successive observation ribbons acquired by Juno. Light curves are then constructed, and the longitudinal shift between the brightness and color ratio peaks is measured. A statistical analysis of these shifts, as well as of event occurrence, is performed as a function of longitude, local time, radial distance, and hemisphere.

The analysis reveals clear hemispheric asymmetries in Jupiter's auroral dynamics. Small-scale structures dominate overall. In the Northern Hemisphere, fewer structures are detected between 135°–180° longitude. In the Southern Hemisphere, structure occurrences increase between 12:00 and 03:00 LT, whereas in the north this increase occurs later. Positive longitudinal shifts between brightness and color ratio peaks are rare, in contrast with earlier studies. Observed negative and no-shifts are consistent with energy-dependent particle dynamics: populations remain together for no-shifts, while higher-energy particles start drifting for negative shifts. These results suggest that previous reports of frequent positive shifts were influenced by methodological biases, and they highlight the combined role of magnetic field asymmetries and dynamic plasma processes in shaping auroral variability.

Acknowledgements

I sincerely thank my supervisor, Bertrand Bonfond, for his patient guidance, insightful advice, and availability throughout this project. His expertise has been invaluable in helping me navigate the challenges of this research and pursue rigorous scientific work.

I am grateful to Linus Head for his invaluable assistance with the coding aspects of this project. His guidance significantly improved the quality and efficiency of the coding work. His patience and willingness to help whenever needed made the process much smoother. I would like to thank Prof. Dominique Sluse for taking the time to discuss a specific method with me and for providing valuable insights, which helped guide my own approach to determining the structure size using Python.

I wish to express my gratitude to my family for their constant support and encouragement throughout this project. Their belief in me, patience during long hours of work and understanding of the demands of this research have been a great source of motivation, enabling me to complete this project.

I am grateful to my friends, Laura, Basile, Vincent, Morgane and Ioana for their support and the enjoyable moments we shared over the past two years. Their encouragement, humor, and team spirit have greatly enriched this experience and helped me stay motivated throughout the program.

Contents

Chapter 1

Context

1.1 Jupiter

Jupiter is the fifth planet from the sun in the solar system. It is one of the gas giants and the largest planet orbiting the Sun. Jupiter orbits at a distance of 5.2 astronomical units (AU) from the Sun, compared to Earth's 1 AU. Due to its rapid rotation, with a period of 9 hours and 55 minutes, this planet is noticeably flattened at the poles and bulging at the equator. It takes 12 Earth years to complete one orbit around the Sun. Unlike Earth, Jupiter has no solid surface. Its gaseous composition makes it difficult to define a clear boundary between its atmosphere and what might be considered a surface. Scientists define Jupiter's surface as the layer where atmospheric pressure is equal to that on Earth at sea level (Encrenaz 1999).

Jupiter's mass is 318 times greater than Earth's, resulting in a stronger gravitational attraction. Similar to the other gas giants, Jupiter possesses a system of rings and a large number of natural satellites. 97 moons were discovered around this planet, four of them are comparable in size to planets: Io, Callisto, Europa and Ganymede (*Planetary Satellite Discovery Circumstances* 2025).

The study of Jupiter's atmosphere is a key to understanding other planetary atmospheres. The stability and/or evolution of atmospheres, as well as interactions with the outside, such as the ionosphere and magnetosphere, and the inside, are controlled by the same processes.

1.1.1 Jupiter's atmosphere

An atmosphere can be defined as a thin layer of gas surrounding a planet. On Earth, the atmosphere allows us to breathe by providing us with air and protecting us from the sun's UV rays. Without this layer of atmosphere, the difference in temperature between night and day would be much greater than what it is now. The atmosphere is divided into 5 layers: troposphere, stratosphere, mesosphere, thermosphere and

exosphere (Saha et al. 2008). The Earth's atmosphere includes nitrogen, oxygen, carbon dioxide, argon and other gases present in smaller quantities.

On Jupiter, the atmosphere can be divided into several layers. The troposphere is the layer at the planet's surface level, where the pressure is 1 bar. The stratosphere of Jupiter is the atmospheric layer located above the tropopause, which occurs around 100–300 mbar, and below the base of the high-temperature thermosphere, near 10^{-3} mbar (Moses et al. 2004). Within the stratosphere, temperatures rise with altitude due to the absorption of solar radiation by methane in the near-infrared. Cooling occurs primarily through radiative emissions from methane and other hydrocarbons such as ethane (C_2H_6) and acetylene (C_2H_2). The sharp temperature increase near the top of the stratosphere is linked to the reduced abundance of hydrocarbons at higher altitudes, as these heavier molecules become separated by diffusion. Jupiter's thermosphere is the planet's outermost atmospheric layer, where densities are extremely low and hydrogen (H_2) is the dominant component, while helium (He) remains largely inert (Yelle et al. 2004). This layer absorbs solar extreme ultraviolet (EUV) radiation and energetic particles from the magnetosphere, leading to molecular dissociation and ionization. In this region, molecular diffusion outweighs convective mixing, and thermal conduction plays a role in the energy balance. The ionosphere develops within the thermosphere as a result of these ionizing processes. Long-lived H^+ ions accumulate because they do not readily react with H_2. The exosphere forms the outermost part of the atmosphere, defining its upper limit (Pierrard 2009).

Jupiter's atmosphere is most striking for its vivid stripes: alternating light and dark bands that wrap around the planet from east to west (Vasavada et al. 2005). These are known as zones (lighter) and belts (darker), separated by powerful jet streams blowing in opposite directions. Zones tend to be cloudier and more reflective, while belts are thinner in clouds, darker in appearance, and allow more heat to escape (Irwin et al. 2001). In the zones, the winds circulate in an anticyclonic pattern, with an eastward jet stream on the poleward edge and a westward one on the equatorward edge (Ingersoll et al. n.d.). In contrast, the belts are cyclonic, rotating in the opposite direction to the zone. Within this restless system, Jupiter also hosts swirling vortices and long-lived storms, the most famous being the Great Red Spot, a massive and centuries-old anticyclonic vortex.

Beneath these visible patterns lies an atmosphere made mostly of molecular hydrogen and helium, with a small share of methane and only trace amounts of other elements (Encrenaz 1999; Atreya et al. 2003). The cloud layers stack up in distinct tiers: the deepest and thickest are thought to be water clouds, above which form clouds of ammonium hydrosulfide, produced when hydrogen sulfide reacts with ammonia. The condensation of pure ammonia creates layers of NH_3-ice clouds (Atreya et al. 1999).

1.1.2 Jupiter's magnetosphere

Jupiter possesses the strongest magnetic field of all the planets, along with the largest magnetosphere and the most powerful radiation belt (Bolton et al. 2015). According to Khurana et al. (2004), "a magnetosphere is defined as a "sphere" of influence around a planet in which the forces associated with the magnetic field of the planet prevail over all other forces". Three key elements are essential for the formation and maintenance of Jupiter's magnetosphere. First, a strong magnetic field is necessary to counter the effects of the solar wind. This magnetic field creates a boundary known as the magnetopause, which separates the magnetosphere from the interplanetary medium. This thin layer is crossed by substantial surface currents and separates the plasmas of the solar wind and the magnetosphere. Secondly, there must be an internal or external plasma source to populate the magnetosphere. The primary source of plasma is located within the magnetosphere itself. Notably, Jupiter's moons and ionosphere contribute to this process, bringing plasma into the magnetosphere. Observations made from the Voyager spacecraft revealed that Io is the main source of plasma in Jupiter's magnetosphere. The volcanic activity on Io produces sulfur dioxide and sulfur, which ionize and decompose to form sulfur and oxygen ions, key components of the plasma in Jupiter's magnetosphere. Finally, the magnetosphere requires a source of energy, which for the rotational magnetosphere comes from the planet's rapid rotation.

Earth's magnetospheric plasma mainly consists of ions and electrons. Those particles originate from both the solar wind and the Earth's ionosphere. Within the magnetic field of Earth's magnetosphere, high-energy particles (with energy in the keV range) gyrate around the magnetic field lines, bounce along them and drift around the Earth. Ions drift toward the west while electrons drift toward the east. In regions with a pressure gradient, the combined effects of particle drift and gyration motion lead to a net charge transport and the formation of a ring current around the Earth (Ganushkina et al. 2018). Galileo observations showed the existence of similar current systems in Jupiter's magnetosphere (Khurana et al. 2004).

Several currents can be identified within the magnetosphere of Jupiter (Khurana et al. 2004; Kivelson 2005; Ganushkina et al. 2018). The magnetopause current is a surface current that flows along the magnetopause and is driven by the confinement of the magnetic field within a cavity in the solar wind, caused by the interaction between the magnetic field and the solar wind flow. On the nightside of Jupiter, the magnetotail current consists of two distinct components. The first part of the current in the magnetotail flows from dawn to dusk through the center of the tail, while the second forms a loop above and below the tail's center.

Field-aligned currents in Jupiter's magnetosphere serve two primary roles: they support the partial ring current by connecting to the ionosphere, and they also electrically link Jupiter's ionosphere to its moons, including Io. These currents must traverse regions with low carrier density and complex force balances between centrifugal pressure and Jupiter's gravity.

Jupiter's current sheet comes from near the Io's orbit, where magnetic forces hold the dense plasma torus against the centrifugal force experienced by the corotating

plasma. The position of the current sheet can shift due to solar wind pressure. Within about 30 RJ, the sheet tends to follow Jupiter's magnetic dipole equator, but farther out, it aligns more closely with the planet's geographic equator. In the distant magnetotail (beyond 60 RJ), it runs parallel to the direction of the solar wind flow.

Radial currents at Jupiter help maintain plasma corotation and generate auroral emissions by accelerating electrons into the ionosphere. They also participate in current circuits linking Jupiter to its moons, notably Io, exerting forces that attempt (unsuccessfully) to alter their relative motion. These currents operate across regions with low plasma density and competing gravitational and centrifugal influences.

All these currents flow in the opposite direction to the corresponding currents found in Earth's magnetosphere due to a difference in dipole orientation between the two planets (Kivelson 2005), as illustrated in Figure 1.1.

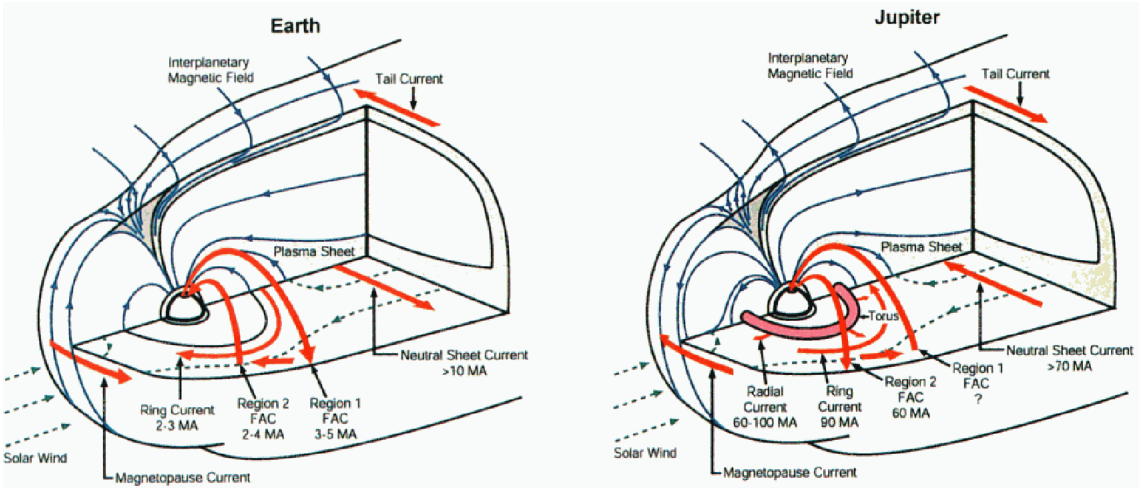

Figure 1.1 Illustration of the current systems in Earth's (left) and Jupiter's (right) magnetosphere made by Khurana (2001)

In the opposite direction to the Sun, the magnetosphere of Jupiter extends outward and forms a tail while the side facing the Sun is compressed. A schematic representation of this giant planet's magnetosphere can be seen on Figure 1.2. The low solar wind density at a distance of 5 astronomical units (AU), combined with the presence of a strong internal magnetic field and plasma pressure within the magnetosphere contributes to the large size of the magnetosphere (Kivelson et al. 2014). The magnetosphere can be divided into three distinct regions: the inner, middle, and outer magnetosphere (Khurana et al. 2004). These regions are identified by two transition zones located between 10-15 Jupiter radii (Rj) and 40-60 Rj.

The inner magnetosphere is closest to Jupiter and contains the planet itself along with its moon, Io, which is the primary source of plasma in the magnetosphere. This region consists of charged particles that are trapped along dipolar magnetic field lines. Radiation belts are created in this inner magnetosphere by the energization of inward-diffusing plasma by electric fields. Between radial distances of 5.2 and 10 Rj lies Io's plasma torus. This region contains several million tons of plasma that diffuse slowly outward, partially due to instabilities driven by the centrifugal force.

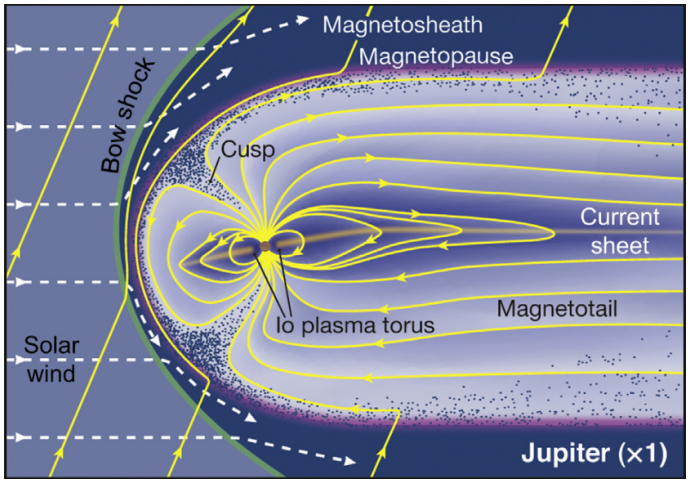

Figure 1.2 Schematic representation of Jupiter's magnetosphere produced by Steve Bartlett Kivelson et al. (2014)

The middle magnetosphere is characterized by a radial stretching of the magnetic field. In this region the centrifugal forces resulting from Jupiter's rapid rotation cause the magnetosphere to take on the shape of a magnetodisc. The further away from Jupiter, the greater the angular momentum required to maintain the plasma. After 30-40 Rj, Jupiter's ionosphere is no longer sufficient to support the angular momentum of the outflowing plasma. This behavior implies a gradual interruption of plasma corotation with the magnetosphere in this region, characterized by an angular velocity that is less than Jupiter's angular velocity.

The outer magnetosphere is the region located beyond 40-60 Rj. In this area, the azimuthal plasma velocity lags behind corotation by a factor of two or more. On the day side, the magnetosphere is flexible, changing in size according to the dynamic pressure of the solar wind. The front of the magnetopause can reach distances of 45 Rj to 100 Rj. In contrast, on the night side, the magnetic field lines are elongated by the magnetotail current system. This current system connects the magnetodisc current to the magnetopause current, resulting in the formation of a long magnetotail that can extend as far as Saturn's orbit.

1.2 Color Ratio

Spectra derived from data collected by the Low spectral resolution Voyager Ultraviolet Spectrometer indicate the presence of methane absorption at specific wavelengths (Broadfoot et al. 1981). This molecule partially absorbs hydrogen molecular (H_2) emissions at wavelengths shorter than 140 nm. In contrast, emissions at longer wavelengths (between 155 and 170 nm) remain unaffected by the presence of hydrocarbons.

The color ratio was originally described by Yung et al. (1982) as follows:

$$CR = \frac{I(155-162)}{I(123-130)}$$

Here I(155-162) represents the intensity (in photon units) integrated from 155 to 162 nm while I(123-130) is the total intensity between 123 and 130 nm. Subsequent studies revealed that the original denominator range could not be reliably used, due to calibration uncertainties resulting from gain loss encountered by Juno/UVS in the vicinity of the Lyman-α line in the detector's wide-slit region (Benmahi et al. 2024). Consequently, the denominator is now calculated using the 125-130 nm range :

$$CR = \frac{I(155-162)}{I(125-130)}$$

This adjustment ensures that the color ratio is based on a wavelength interval with accurate and trustworthy instrument calibration. The numerator therefore corresponds to the unabsorbed emission band, whereas the denominator relates to the band where CH_4 absorbs. In the absence of hydrocarbon absorption, the color ratio has a value of approximately 1.1 (Gérard et al. 2016).

When combined with an electron transport model, the far-ultraviolet (FUV) color ratio can be employed to determine the characteristic energy of the auroral precipitation. Energetic particles penetrate deep into Jupiter's atmosphere. The resulting photons are preferentially absorbed by methane at wavelengths shorter than 140 nm (Gladstone et al. 2017b).

The Space Telescope Imaging Spectrograph aboard HST has been used to create the first FUV spectral maps of the Jovian aurora as demonstrated by Gérard et al. 2014. These maps reveal that the amount of methane absorption varies across different regions. The polar emissions and those from the main oval exhibit the highest color ratios, indicating the greatest levels of auroral precipitation.

Brightness maps are constructed using detections in the wavelength range 155-162 nm. Color ratio maps are based on two detections: one in this wavelength range and the other in the wavelength range 125-130 nm. These maps are obtained by dividing the first wavelength range by the second.

1.3 Jupiter's aurorae

Auroras are emissions produced by the interaction between a planet's upper atmosphere and energetic charged particles. Auroral emissions can occur in the ultraviolet (UV), visible (VIS), and X-ray ranges. Jupiter, known for having the most intense auroral activity, displays particularly spectacular auroras in terms of both scale and complexity.

1.3.1 Aurora formation

Auroras are caused by the interaction of several key factors. First and foremost, the planet's atmosphere plays a crucial role due to its composition. The chemical composition of a planet's atmosphere determines which wavelengths are emitted during auroral processes. A second essential element is the presence of a magnetic field, which guides charged particles. Finally, plasma composed of energetic charged particles completes the process.

Some planets, including Earth, Mercury, and the gas giants, are capable of generating a magnetic field (Stevenson 1983). The lines of this magnetic field extend around the planet but are invisible to the naked eye. The magnetosphere is the region of space where a planet's magnetic field dominates over the solar magnetic field. For the Earth, this region is elongated in the opposite direction to the Sun and compressed on the side facing the Sun. Local time asymmetries are observed in Jupiter's magnetosphere (Khurana et al. 2004). This asymmetrical shape results from the interactions with the solar wind, as explained in the previous section.

The plasma is the fourth state of matter composed of charged particles such as ions and electrons. Charged particles can be found in the magnetosphere of a planet due to ionization and impact (Khurana et al. 2004). On Earth, plasma primarily originates from the ionized outer layers of the atmosphere, known as the ionosphere, as well as from particles emitted by the Sun and carried by the solar wind. The Sun contains regions characterized by a powerful magnetic field that release charged particles. In contrast, the plasma around Jupiter is supplied both by the solar wind and Io, one of its moons. This satellite is characterized by numerous volcanoes that eject particles into space. Jupiter's powerful magnetic field traps these charged particles.

1.3.1.1 Acceleration mechanism

The precipitation of electrons and ions from the magnetosphere to the atmosphere can result from multiple mechanisms. The following discussion focuses on two of the most important mechanisms responsible for this particle precipitation.

1.3.1.1.1 Alfvénic auroral acceleration

Auroral particle acceleration by Alfvén waves involves a sequence of physical processes that connect the outer magnetosphere to the ionosphere (Lysak 2023). The first step is the generation of Alfvén waves in the outer magnetosphere. These waves, originally described as shear mode waves (Alfvén 1942), propagate along magnetic field lines and act as a mode of ideal magnetohydrodynamics (MHD). They efficiently transfer both energy and field-aligned currents toward the ionosphere, carrying a net Poynting flux that supplies the energy needed for particle acceleration. The field-aligned currents transported by these waves must be closed through the ionosphere.

As Alfvén waves travel inward, their perpendicular wavelength can decrease, leading to the formation of kinetic Alfvén waves. These kinetic waves are characterized by a parallel electric field, which plays a crucial role in accelerating particles. Strong plasma density gradients near the ionospheric boundary further influence the interaction of these waves with the ionosphere. These gradients act as an effective resonator, generating rapid fluctuations on time scales of seconds. The ionosphere itself reflects part of the wave energy, contributing to the confinement and amplification of these oscillations.

These rapidly varying parallel electric fields can stochastically accelerate auroral electrons across a broad energy range, a phenomenon commonly referred to as the Alfvénic aurora. Moreover, coupling between Alfvén surface modes and kinetic Alfvén waves can lead to additional heating and particle acceleration.

Saur et al. (2003) proposes that weak magnetohydrodynamic (MHD) turbulence in Jupiter's middle magnetosphere interacts with the large-scale electric current system responsible for maintaining magnetospheric corotation. This interaction is believed to generate a field-aligned electric potential drop that accelerates magnetospheric electrons to the energies needed to produce Jupiter's main auroral oval.

A key distinction between Jupiter's and Earth's magnetospheres is the presence of a strong internal plasma source: Io. The plasma generated near Io's orbit corotates with Jupiter and is transported outward through a process called interchange transport, driven by centrifugal forces. As the plasma moves outward, maintaining corotation requires a continuous transfer of angular momentum from Jupiter to the plasma, achieved via a large-scale current system.

In this system, the magnetospheric plasma, mainly located near the magnetic equator, is accelerated by the $\mathbf{j} \times \mathbf{B}$ force resulting from electric currents that flow between Jupiter's ionosphere and its magnetospheric plasma sheet. These field-aligned currents, also known as Birkeland currents, are assumed to flow without resistance. Subsequent studies (Hill 2001; Cowley et al. 2001) linked the upward field-aligned current regions to the location of Jupiter's main auroral oval. The authors argue that the required field-aligned potential drop may result from the coupling between this current system and weak MHD turbulence observed in the middle magnetosphere.

In a collisionless plasma like Jupiter's, field-aligned currents must propagate via shear Alfvén waves, which transmit net current between the ionosphere and magnetosphere. The turbulent fluctuations, which are nearly incompressible, propagate along magnetic field lines and interact nonlinearly, producing a cascade of energy to smaller scales. Eventually, this energy is dissipated through Joule heating at kinetic scales, leading to what the authors refer to as "anomalous turbulent resistivity." In the presence of a net current, this resistivity generates a background electric field, which in turn creates a field-aligned potential drop between the planet and the magnetospheric plasma. This potential drop enables the acceleration of electrons toward Jupiter's atmosphere.

Kinetic Alfvén waves play a central role in the process of particle acceleration, facilitating the transfer of energy from electromagnetic fluctuations into energetic auroral

electrons.

1.3.1.1.2 Pitch-angle scattering into the drift loss cone

Within Jupiter's magnetosphere, charged particles such as electrons and ions are trapped by the planet's magnetic field. These particles exhibit three combined motions. First, they undergo gyration around the magnetic field lines. The second motion is bouncing: particles oscillate between two mirror points, located in regions where the magnetic field is stronger. At these points, particles are reflected and travel back in the opposite direction along the magnetic field lines. Finally, drift is a slower motion by which the particles move around the planet. For positively charged ions, the drift occurs eastward, while for negatively charged ions and electrons, it is directed westward.

The gyration motion is characterized by the pitch angle, defined by Abel et al. (2003) as 'the angle of the particle's trajectory relative to the magnetic field line as it crosses the equatorial plane'. Initially, many particles have a pitch angle close to 90°, corresponding to a large velocity component perpendicular to the magnetic field, resulting in pronounced gyration around the field lines. The pitch angle distribution then takes a pancake shape.

Following a disturbance, the pitch angle distribution may become bidirectional, with smaller pitch angles. Tomás et al. (2004) mentions two mechanisms that could be responsible for this change in the pitch angle distribution. The first is increased scattering of locally trapped particles toward smaller pitch angles as a result of enhanced wave activity in the region, potentially driving the distribution toward the strong pitch-angle diffusion limit. The second involves the outward transport of particles from the radiation belts without significant energy loss, including low-altitude scattering that diffuses particles toward higher latitudes, thereby producing a bidirectional anisotropy.

Particles retain their gyration motion, although it is less pronounced than in the pancake distribution. They then have a large velocity component parallel to the magnetic field and a small component perpendicular to it.

The loss cone is defined as the range of pitch angles below which the planet's magnetic field cannot magnetically reflect charged particles because their mirror points lie within the upper atmosphere. Particles with pitch angles within this loss cone have theoretical mirror points located deep within the upper atmosphere. As a result, these particles do not undergo magnetic reflection in the magnetosphere because they reach the atmosphere before encountering a strong enough magnetic field to be reflected. Consequently, they precipitate into the atmosphere where they can collide with neutral particles.

1.3.1.2 Auroral emissions

Disturbances in the plasma can cause some of these charged particles to accelerate and precipitate along magnetic field lines toward the upper atmosphere. When they collide with atmospheric atoms and molecules, they produce auroral emissions through various physical processes (Bhardwaj et al. 2000).

The first noticeable process is electronic excitation, where an electron in an atom or molecule absorbs energy and transitions to a higher energy level. The second process is ionization in which an electron is eventually ejected from the atom or molecule. Finally, there is dissociative excitation, which causes a molecule to break apart as a result of a collision. These processes are often followed by de-excitation of these atoms or molecules during which electrons return to lower energy states and emit photons, producing light at specific wavelengths.

On Earth, charged particles collide with gases in the atmosphere, which is primarily composed of oxygen and nitrogen (Helmenstine 2023) producing auroras in the ultraviolet (UV), visible (VIS), InfraRed (IR) and radio wavelengths. The latter emissions result from interactions between electrons and electromagnetic waves at high altitudes. The UV auroras, on this planet, are green when high-energy electrons collide with monoatomic oxygen, and they appear red when lower-energy electrons collide with monoatomic oxygen and diatomic nitrogen. Collisions with diatomic nitrogen produce blue emissions. Mauve, pink and white hues can also be detected by their mixture.

On Jupiter, auroras are the result of collisions between energetic particles and hydrogen or helium, the most abundant species in Jupiter's upper atmosphere. The excited hydrogen releases energy in the form of emissions in the Lyman, Werner, and Rydberg bands of H2 and the Lyman series of H (Lyα)(Hue et al. 2019). When excited, molecular hydrogen emits predominantly in the ultraviolet (UV) range. Since Jupiter's atmosphere is primarily composed of molecular hydrogen, its auroras are especially intense in UV. Apart from its auroral activity, Jupiter neither emits nor reflects ultraviolet radiation. This means that the UV auroral emissions appear against a dark background, which makes them easier to analyze.

While Jupiter's auroras are mostly studied in the ultraviolet and infrared wavelengths, they also produce visible light auroras. These visible glows arise when energetic particles collide with molecular hydrogen, causing it to break apart and emit light in the Balmer series, along with additional emissions from excited hydrogen molecules (Waite Jr et al. 2000). However, because sunlight scatters in Jupiter's atmosphere, these visible auroras can only be seen on the planet's nightside. The Galileo spacecraft observed these auroras using several filters : the violet filter (385-430 nm), green (520–600 nm), red (625–705 nm), methane (875–900 nm), near-infrared (950–1050 nm) and a clear filter (385–935 nm) (Ingersoll et al. 1998). Auroral emissions were detected in all filters except the near infrared 968 nm, where no detectable auroral emission was detected. High-resolution images revealed distinct features such as a main auroral ring extending around the planet, localized bright spots near the limb, and fluctuating patches both north and south of the main emission.

1.3.2 Auroral Morphology

The figure 1.3 illustrates the main far-ultraviolet (FUV) auroral features typically observed in Jupiter's Northern Hemisphere from Earth orbit. The different components are projected onto an orthographic polar map for clarity. The upper gray-shaded area indicates the region that remains out of view for Earth-orbiting observatories such as HST.

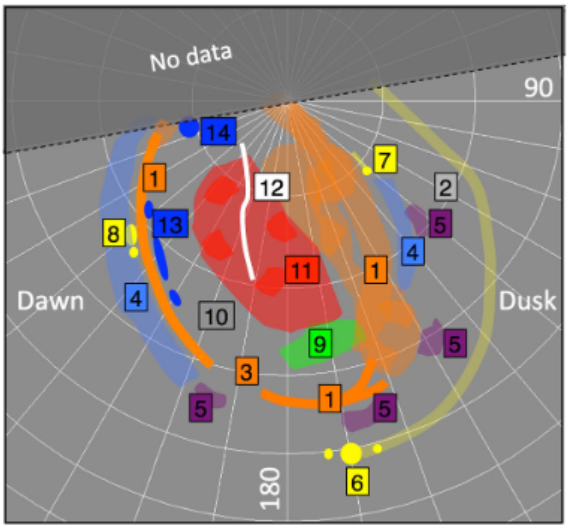

Figure 1.3 Visualization of the northern components of Jupiter's FUV aurora .1: Main emission (oval); 2: Kink region; 3: Discontinuity; 4: Secondary emission; 5: Signatures of injections; 6: Io footprint (multiple) and tail; 7: Europa footprint and tail; 8: Ganymede footprint (multiple); 9: Polar active region; 10: Polar dark region; 11: Polar swirl region; 12: Polar auroral filament (PAF); 13. Dawn spots and arcs; 14: Midnight spot. (Grodent 2015)

Generally, the dawnside aurora forms a narrow, nearly continuous arc in UV images. Around local noon, the emission becomes more fragmented, consisting of discrete auroral patches. On the dusk side, the aurora tends to widen and separate from the main emission region. The nightside polar area of Jupiter is not observable from Earth orbit.

Following a nearly simultaneous analysis of the HST images of Jupiter's two hemispheres, Gérard et al. (2013) discovered that the majority of the morphological characteristics of aurorae identified in one hemisphere had a conjugated counterpart in the other hemisphere. It is also noted that there are power disparities related to conjugated regions. Jupiter exhibits several regions of auroral emission, distinguished by their locations, the physical processes and source regions from which they originate, as well as their temporal variations (Clarke et al. 2004). These different emissions can be classified into 3 groups (Bonfond et al. 2017a), as illustrated on Figure 1.4. In addition to these regions, Jupiter's aurora also includes another distinct contribution: the footprints of its moons.

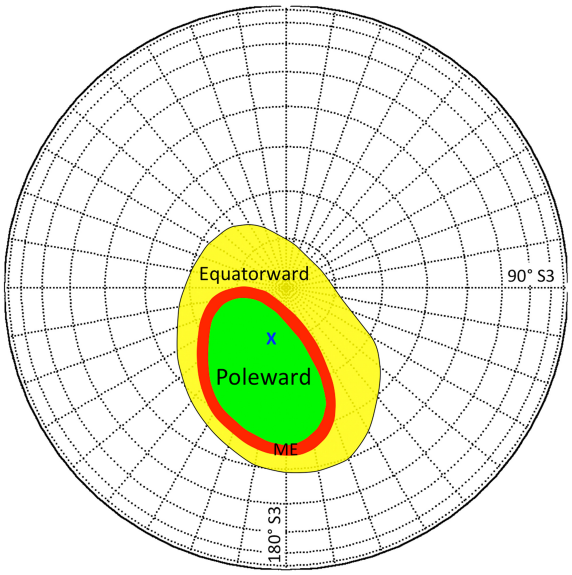

Figure 1.4 The figure, realized by Grodent et al. 2018, illustrates the three main subregions of Jupiter's northern aurora: (1) the main emission (ME, red), also known as the main oval; (2) the polar or poleward region (green); and (3) the equatorward region (yellow), defined by the equatorward boundary of the main emission and encompassing the footprints of Jupiter's satellites.

1.3.2.1 The main emission

The main emission, also called the main oval (Clarke et al. 2004), is relatively stable and irregular. It is characterized by a patchy or segmented structure and varies on a timescale ranging from 10 minutes to several hours (Grodent et al. 2003). Combining data from Juno and HST, Yao et al. (2022) examines changes in Jupiter's auroral pattern. When the magnetosphere is compressed by the solar wind, Magnetospheric Auroral Brightening (MAB) events occur, which are absent during times when the magnetosphere is expanded. The main auroral emissions become stronger, especially in the morning and afternoon sectors, causing a near-noon discontinuity that shifts from around 10 LT during calm periods to about 12 LT during MAB events. Conversely, during expanded magnetospheric conditions linked to lower solar wind pressure, the aurora appears either dim or shows Auroral Dawn Storm (ADS) activity, with no dimming seen during compression. These results demonstrate a clear connection between solar wind-driven compression of Jupiter's magnetosphere and the brightness and structure of its main aurora.

The main auroral oval is a ring-shaped region that encircles Jupiter's north and south poles. This area is positioned between the polar emission and the footprint of Io and observed at a dipolar latitude of approximately 15° (Cowley et al. 2001). Magnetic field modeling analyses indicate that this emission is linked to field lines that extend to the Jovian equator, reaching over 20 radii from Jupiter.

While the main auroral oval is essentially continuous throughout local time, the width and intensity of this emission can vary. The main auroral oval is confined to a narrow band but exhibits a bright appearance. A discontinuity has been identified in Jupiter's main auroral oval, where the emission intensity falls to less than

10% of its maximum value. This feature is observed in the Northern and Southern Hemispheres. Images taken at various central meridian longitudes indicate that the discontinuity remains fixed in magnetic local time. The origin of this discontinuity, based on observations, theoretical considerations and magnetohydrodynamic simulations, is thought to be linked to weakened and/or downward field-aligned currents (Radioti et al. 2008). The mechanism underlying the main auroral oval emission remains incompletely understood. Over the years, several hypotheses have emerged.

Tsurutani et al. (1997) proposed that this emission was due to wave diffusion of magnetospheric plasma in the magnetopause boundary layer. According to this theory, after being scattered in pitch angle into the atmospheric loss cone, energetic particles are guided by magnetic field lines down to Jupiter's ionosphere/atmosphere, where they produce auroral emissions via collisions. However, although a weak high-latitude auroral ring can be formed with the energy precipitation rate, the intensity is too low to generate the main aurora emission.

Cowley et al. (2001) suggested that the main auroral oval is associated with coupling currents between the magnetosphere and ionosphere, which are linked to the breakdown of corotation in the middle magnetosphere. Bonfond et al. (2020) provided an overview that includes hypotheses and counterarguments related to the formation of Jupiter's main oval by those coupling currents. Several observations began to contradict the predictions.

An alternative model was proposed by Saur et al. 2018 explains the origin of this main emission associated with Jupiter's magnetosphere. According to this model, the radial transport of plasma leads to small-scale magnetic field perturbations within Jupiter's magnetosphere. These disturbances propagate along the planet's magnetic field lines as Alfvén waves, which can be partially reflected at density gradients. The reflected waves then interact with each other in a nonlinear manner, resulting in a turbulent cascade of fluctuations toward progressively shorter wavelengths. As the wavelength approaches the kinetic scales of magnetospheric particles, the cascading Alfvén waves can undergo wave-particle interaction through Landau damping. This process converts wave energy into plasma heating and particle acceleration onto the ionosphere. The resulting acceleration is stochastic rather than unidirectional. Within a L-shell of 30 RJ, the population of energetic electrons contributes to the formation of Jupiter's main auroral oval.

1.3.2.2 The outer emission

Secondary auroral emissions appear at latitudes situated between the main emission and the Io footprint, specifically equatorward of the main emission and poleward of the Io footprint (Radioti et al. 2009). These emissions manifest as extended features stretching from the main emission toward lower latitudes, sometimes forming discrete arcs parallel to the main emission or irregular, patchy diffuse structures (for example, the light blue diffuse arcs). Additionally, these emission may present as isolated features, which have been associated to injections of hot plasma in the middle magnetosphere. Collectively, these phenomena constitute what is known as

the equatorward diffuse emissions (EDE).

The persistent nature of the EDE suggests a connection with a stable magnetospheric structure, such as the pitch angle diffusion (PAD) boundary (Grodent 2015). Other diffuse emissions might arise from different processes, including electron scattering by whistler-mode waves associated with anisotropic injection events.

Plasma injection signatures have been identified as distinct structures within the outer emission. These structures are compact auroral features that refer to an increase in high-energy particle populations that move azimuthally around the planet, guided by magnetic field gradients and curvature. Their motion is influenced by their charge, mass and energy in a colder plasma. At Jupiter, two possible mechanisms, originally identified from studies of Earth's magnetosphere, have been proposed by Mauk et al. (2002) to explain how injected particles could produce auroral emissions. In the first, the energy distribution of the particles becomes unstable during injection, allowing wave–particle interactions that scatter some particles along magnetic field lines until they meet the atmosphere. In the second mechanism, electric currents flow along the boundaries of the injected particle cloud. Variations in magnetic field strength with radial distance cause these currents to diverge at the cloud's leading and trailing edges. These currents can interact with plasma near the planet and lead to downward accelerated electrons.

Bonfond et al. (2017a), using Juno-UVS data, reported that several auroral features associated with plasma injections exhibited a shift between their brightness and color ratio peaks. During her PhD, Maïté Dumont investigated these shifts (Dumont 2023). Shifts can be computed by identifying the difference in longitude where the intensity reaches its maximum in the brightness and color ratio maps. Three types of shifts can occur: positive, negative, and null when considering the difference between the longitude of the peak in the brightness' map and that in the color ratio map. A margin of error of $\pm 0.9^\circ$ is used to identify null shifts. Relative to the rotation of the plasma around Jupiter, a negative shift is observed downstream the brightness peak. Both negative and zero shifts result from plasma injection events, where particles of different energies drift at varying rates due to magnetic field gradients and curvatures. The differential drift between low- and high-energy particles is therefore responsible for the shift between the brightness peak and the color ratio peak. For cases with no shift, the particle populations remain together, so the brightness and color ratio peaks coincide. In contrast, for negative shifts, the higher-energy particles have already started their differential drift, which produces the observed negative shift between the brightness peak and the color ratio peak.

The findings of her thesis suggest that, over time, low-energy and high-energy electron populations progressively separate, resulting in negative shifts. This happens because high-energy electrons drift faster in longitude. Null shifts are linked to recent plasma injections, during which the electron distribution remains uniform. As a result, the shift appears null because the injected population has not yet had time to segregate. Positive shifts, in contrast, are thought to be related to the method used to construct the maps. During a perijove, Juno cannot observe all auroral emissions instantaneously. It is therefore necessary to assemble several spins to obtain a complete map. Master maps, used in this study, are created by combining

non-simultaneous observations, which means that plasma injections occurring at a specific time (t) may have evolved and thus can be found at a different longitude than the one where they were originally injected. This temporal mismatch can artificially produce a positive shift.

1.3.2.3 The polar emission

Polar auroral emissions are located at the pole of the main auroral emission. Although the origin of these emissions has not yet been definitively established, they are linked to the dynamics of the outer magnetosphere and depend on magnetic local time (Greathouse et al. 2021). There is a transition region between the polar emission and the main emission that is called the Polar Collar. This area lies within the auroral oval and its brightness changes depending on the local time in the magnetosphere (Greathouse et al. 2021). This type of emission varies very rapidly, typically on the order of tens of seconds. This variation is likely connected to reconnection areas near the flanks of the magnetotail or the dayside magnetopause (Gladstone et al. 2017a).

The polar emission can be divided into three regions. The differences between these three regions stem from their distinct morphologies and observed dynamic behavior. The first notable zone, known as the 'dark region', is nearly devoid of auroral emissions. This region is bounded on the one hand by the main oval on the equatorial side and on the other by the two other distinct regions that make up the polar emission. The second zone, referred to as the swirl zone in the Northern Hemisphere, can be defined as an area characterized by weak, patchy, and transient emission features, which are typified by turbulent motions that sporadically create localized clockwise swirls. The swirl region is located around the center of the polar region and occupies approximately one-third of the area bounded by the main oval. The third region is the "active region", which consists of two different types of emissions. It includes bursts that may result from polar flares, which are bright and brief occurrences (Grodent et al. 2003). The second type of emission constituting this area are the "bridges". These emissions are auroral arcs observed in Jupiter's polar region that stretch across the polar collar, forming a connection between the main emission and the dayside active region. These features lie within the polar aurora and are thought to map to distant areas of Jupiter's magnetosphere (Head et al. 2025).

1.3.2.4 The satellites footprints

As the name suggests, the satellite footprints are related to Jupiter's satellites. These emissions originate from the excitation of strong Alfvèn waves that travel along magnetic field lines toward the planet (Bonfond et al. 2024). These waves are excited by the moon's motion through the magnetospheric plasma. These emissions remain fixed along the magnetic flux tubes connected to Io, Europa, and Ganymede (Grodent et al. 2003). Jupiter's rapidly rotating magnetospheric plasma interacts with these satellites, generating Alfvén waves that propagate along the magnetic

field lines (Bonfond et al. 2013). These Alfvén waves develop an oscillating electric field along the field lines, due to the strong dispersive effects they undergo at high altitude. The electromagnetic interactions between the moons and the planet result in signatures in Jupiter's aurora, characterized by a series of spots (Bonfond et al. 2017b).

Io footprint is the brightest and is composed of at least three spots. The main Alfvèn wing (MAW) spot is an auroral feature generated by electrons accelerated toward the planet. The second spot is generated by the electrons accelerated by the Alfvèn waves in the opposite direction from the planet. Those electrons create electron beams along the magnetic field lines and cross the equatorial plane. A portion of theses electrons precipitate in the opposite hemisphere creating the Trans-hemispheric Electron Beam (TEB) spot. This feature is found downstream or upstream the MAW spot, depending on the location of Io in the plasma torus. The third spot is the Reflected Alfvèn wave (RAW) spot, caused by the possible transmission of Alfvèn waves that are reflected by the density gradient at the boundary of the plasma torus or the Jovian ionosphere. The RAW spot is located downstream of the MAW spot. Io's spots are followed by a tail that extends downstream with respect to the plasma flow encountering this volcanic moon. It is thought that the tail is created either by repeated reflections of the Alfvèn wave within the torus (Jacobsen et al. 2007) or by parallel quasi-static electric fields linked to large-scale, field-oriented currents between Io's torus and Jupiter's ionosphere (Hill et al. 2002).

The Europa footprint (EFP) is accompanied by an auroral tail, similar to that observed for other satellites such as Io. However, while Io's tail is systematically present, Europa's is rare and difficult to detect. A reanalysis of FUV images taken by the Hubble telescope (STIS and ACS) identified five additional occurrences of the EFP tail, four in the Northern Hemisphere, one in the Southern Hemisphere (Bonfond et al. 2017b). The local interaction of Europa is dominated by an induced magnetic field in contrast to Io's interaction, which is driven by its neutral gas sources. Despite this difference, the EFP has a similar morphology to other footprints, suggesting that a common mechanism is responsible for these auroral trails, regardless of local peculiarities. The process occurring for Europa footprint appears similar to that of Io footprint. The key difference lies in the strength of the interaction between each moon and its environment. The difference factor between these strengths is scaled with the gas/plasma release rate. The gas/plasma escaping from Io is 10 to 20 times the amount of gas/plasma escaping Europa (Grodent et al. 2006).

The location of Ganymede within Jupiter's plasma sheet appears to govern the position of its auroral footprint, which shows brightness variations on timescales of 10–40 minutes and 1–3 minutes. The size of the footprint seems to match that of Ganymede's entire magnetosphere. According to Bonfond et al. (2013), a second Ganymede footprint spot is likely produced by a trans-hemispheric electron beam. This theory was later confirmed by Hue et al. (2022). This secondary spot is observed quasi-systematically in the Southern Hemisphere and only occasionally in the Northern Hemisphere.

Chapter 2

Juno

Juno is the second spacecraft to orbit Jupiter, following Galileo, and it is the first solar-powered mission to the planet. Launched in 2011 as part of NASA's New Frontiers program, Juno entered Jupiter's orbit after a five-year journey (Hue et al. 2019). The spacecraft follows a polar orbit with a period of 53.5 days characterized by a highly eccentric orbit. The closest point of its orbit, known as perijove, is located at 1.05 Jovian radii from the center of Jupiter, while the farthest point, or apojove, is 113 Jovian radii away.

To minimize exposure to Jupiter's harsh radiative environment while enabling close observation of the planet, Juno's elliptical polar orbit allows it to pass through the gas giant's magnetosphere. As can be seen in figure 2.1, Juno rotates around an axis almost perpendicular to the orbital plane at two revolutions per minute in a counterclockwise direction. From Earth's perspective, Juno orbits Jupiter in a clockwise direction (Bolton et al. 2017).

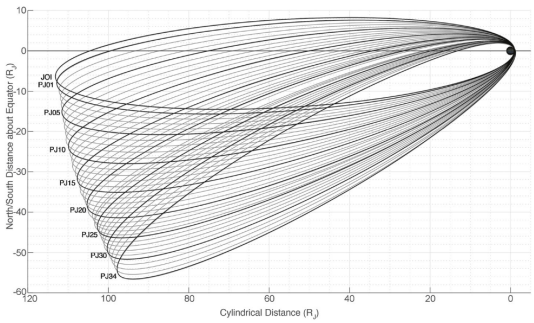

Figure 2.1 Illustration of Juno's path perpendicular to the orbit plane (Bolton et al. 2017)

Juno is equipped with three solar arms, each measuring nine meters in length, which house a total of eleven solar panels. Most of the time, these panels are kept pointed toward the sun, generating a total output of 500 watts. This solar-powered spacecraft is equipped with eight scientific instruments and a proximity camera to study Jupiter and its magnetosphere allowing nine science investigations.

Jupiter's internal structure and magnetic dynamo are reviewed by the Gravity Sci-

ence (GRAV) instrument and the Magnetometer (MAG). The atmospheric composition have been observed using the Microwave Radiometer (MWR). The Juno Energetic Particle Detection Instrument (JEDI) and the Juno Auroral Distributions Experiment (JADE) are used to detect the ion composition and the distribution of auroral particles. Plasma and radio waves were observed by the Waves instrument. Finally, the spatial and temporal structure and dynamics of the atmosphere and aurora were studied using the Ultraviolet Spectrograph (UVS) and the Jovian InfraRed Auroral Mapper (JIRAM). The JunoCam camera, a visible imager, helps to observe the dynamics and structure of the atmosphere. As the instruments look "outwards" in the spin plane, each of them has several opportunities to observe both Jupiter and the space behind (Bolton et al. 2017).

The main objectives of the Juno mission, as outlined by Bolton et al. (2017), include:

- Gaining a better understanding of the formation of giant planets by studying the amount of water in Jupiter's deep atmosphere, the distribution of its internal mass, and its magnetic field.
- Determining the distribution of heavy elements within Jupiter.
- Investigating the magnetic field to reach Jupiter's deep internal dynamics.
- Analyzing deep atmospheric structures.
- Exploring Jupiter's auroras and magnetospheric phenomena.

In the present work, data from the UVS spectrograph onboard Juno were used. This instrument was designed with improvements over its predecessors. A scanning mirror, extensive shielding and a microchannel plate (MCP) detector with crossed delay line (XDL) have been added. The scanning mirror allows the targeting of specific auroral features.

The shielding helps maintain data quality and electronic performance despite the presence of energetic particles in Jupiter's environment. The MCP detector provides faster counting and improved spectral and spatial resolution (Gladstone et al. 2017a; Hue et al. 2019).

Juno's onboard UV spectrograph is designed to focus on auroral features in the far-ultraviolet (FUV) and extreme-ultraviolet (EUV) ranges. It operates as a photon-counting imaging spectrograph with a bandwidth scanning from 68 to 210 nm. This wavelength range covers the UV emissions produced in Jupiter's aurora, including the H_2 bands and H Lyman series, as well as the hydrocarbon absorption signatures (Bonfond et al. 2017a).

The UV instrument consists of a telescope/spectrograph section, where the telescope feeds a circular Rowland spectrograph. As illustrated figure 2.2, it includes a scanning mirror, an entrance aperture, an off-axis parabolic primary mirror, a slit, a grating, and a detector. The slit has a dog-bone shape, with wider outer sections and a narrow central section. Both the scanning mirror and the off-axis parabolic mirror, along with the diffraction grating are crafted from monolithic pieces of aluminum

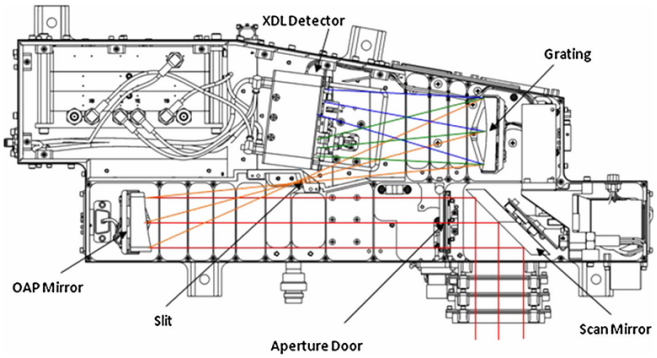

Figure 2.2 The Juno-UVS sensor's opto-mechanical schematic displaying light beams Gladstone et al. (2017a)

that have been coated with electrolytic nickel and polished. To enhance their reflectivity for the specified UV bands, they are also coated with aluminum/magnesium fluoride (AI/MgF_2). The scanning mirror located at the front end of the telescope (Gladstone et al. 2017a) allows for observations up to $\pm$ 30° perpendicular to Juno's plane of rotation, and directs incident light onto the primary mirror (Bonfond et al. 2017a). Following reflection by this primary mirror, the light passes through a 4 x 4 cm^2 entrance aperture and reaches the primary parabolic mirror. The beam is reflected towards the slit and diffracted by the grating towards the detector.

The instrument detects photons at X and Y positions, which correspond, respectively, to the spectral and spatial dimensions along the slit. This configuration allows for the reconstruction of images, taking into account the specific characteristics of the collected data. Several bands, each capturing a part of Jupiter's aurora are obtained (Bonfond et al. 2017a). These bands can then be combined together to create a complete map of Jupiter's aurora.

Chapter 3

Analysis of longitude differences in brightness and color ratio curves

In this work, data from the UVS spectrograph were used to study several characteristics of Jupiter's auroral emissions. The aim of it is to characterize the spatial shift for each plasma injection, called blob in this work, observed during each perijove. As said earlier, the shift can be calculated by identifying the longitude where the intensity reaches its maximum in the brightness and color ratio maps. This process involves computing the light curve of each injection in both maps. The maps used here are constructed with successive ribbons to avoid ambiguities with evolving injections.

This work is divided into several steps. The first step is detecting the structures that make up Jupiter's aurora. This is explained in the first section, where each perijove is analyzed to identify the location of each structure.

The second step involves selecting the structures of interest. This study focuses specifically on the structures found in the outer auroral emissions. Structures found in the polar region, the main auroral oval, and the footprint of Io are not considered relevant for this work. This selection process is described in the second section.

The third step is creating maps. As mentioned earlier, these maps are built using successive ribbons of data. This method is necessary to accurately determine the true size of each structure and the offset between the brightness peak and the color ratio peak.

The fourth step uses the maps constructed in the previous step to measure the size of each structure.

Next, a reference line is created to extract the intensity values of each structure. These values are then plotted as a function of longitude. This process is explained in the following section. In the next step, these plots are used to identify the difference in location between the brightness and color ratio peaks.

Finally, the last step visualizes this shift by generating an image that uses two

different colors to represent the contributions from each parameter.

3.1 Detection

Characterization of Jupiter's outer auroral emissions begins with the detection of plasma injections in Jupiter's aurora.

The detection of structures in images was performed using a Python-based algorithm adapted from the method described by Linus Head (Head et al. 2024). This original method allows the detection of auroral arcs and consists of three main steps. The first one is the preprocessing in which images from Juno-UVS and HST are transformed into 1024×1024 pixel Cartesian polar projections, oriented as if viewed from above Jupiter's northern pole, to enable direct comparison of northern and southern aurorae. The next step is the arc extraction. Auroral arcs are automatically extracted and characterized using a template-matching approach. A 13×13-pixel Gaussian kernel is used to quantify the "arcness" of each pixel in polar-projected images, with the image rotated from 0° to 180° in 1° increments. True auroral arcs are identified by thresholding the arcness map, and skeletonization is applied to extract central axes. Post-processing of the skeleton graph removes very short arcs, resolves intersections, splits edges with small radii of curvature, and merges closely aligned arcs, resulting in a set of detected individual auroral arcs. The final step is the characterization of auroral arcs. Key properties of detected arcs are extracted to analyze arc-like structures in Jupiter's aurorae. Basic properties such as brightness and position are obtained by reprojecting arcs onto polar-projected auroral images, while more complex properties require additional derivations. Magnetic field models (JRM33 for the internal field and Con2020 for the external field) are used to map detected arcs between the ionosphere and magnetosphere, allowing determination of magnetospheric longitudes and local times.

In a subsequent adaptation of this method, Linus Head modified the original arc-detection algorithm to detect blobs, employing a modified range of kernel shapes. In this implementation, images are processed by applying a set of circular Gaussian filters with radii spanning from 7 to 80 pixels. Pixels belonging to areas where the normalized convolution response ("blob score") is greater than 0.6 and the measured brightness exceeds 50 kR are identified as potential blob candidates. In cases where blobs of different apparent sizes overlap, a situation that occurs frequently, the candidate with the highest blob score is preserved.

For each perijove, the algorithm outputs a data array containing the following information for each detected structure:

- The latitude and longitude corresponding to the detection location.
- The size of the detected structure, expressed in pixels, which corresponds to the final diameter of the circular window after expansion.
- The pixel coordinates (x, y) of the center of the structure on the image.

- Additional parameters are also stored, though they were not used in the present study.

This method provides a flexible and scalable approach to structure detection, as it is not limited to features of a fixed size. By using a circular detection window and a tunable intensity threshold, the algorithm can adapt to the varying appearance and contrast of structures across different regions and perijoves.

3.2 Selection of the structure in the outer emissions

During his master thesis, Groulard et al. (2022) analyzed the dawn-dusk asymmetry in the main auroral emission of Jupiter. To accomplish this, he created a mask for each perijove, focusing solely on the emission from the main oval. These masks were generated using specific procedures to filter the relevant emissions.

The construction of the masks for the main emission relied on the reference ovals defined by Bertrand Bonfond, referred to here as B ovals, during the HST 2007 campaign (Groulard et al. 2022). These ovals exhibit different shapes due to the variation in the size of the main emission over time. Brightness peaks were searched for in the vicinity of these B ovals. To avoid including other emissions, additional parameters were introduced. First, the code was set to examine areas outside a region around the barycenter of the main emission. Then, a second parameter allowed the code to search poleward, equatorward, or in both directions. After selecting the best parameters and ovals, the elements were grouped to identify large-scale common brightness structures. Polar-projection maps of the brightness and the B ovals were then generated. These maps were subsequently divided into 3600 sectors around the barycenter of the main emission. For each sector, the barycenter of the B oval was located, and the main emission around that location was examined. If the brightness exceeded a certain threshold, it was considered part of the main emission. If not, the steepest brightness gradient was taken as the signature of the main emission. If no emission was found at all, the search around the center of B oval was expanded. Ultimately, 3600 points representing the locations where the main emission occurs were identified and fitted using a Fourier series. The final step consisted of assigning a width to this curve. The final result is shown in Figure 3.1.

In this work, the masks created by Antoine Groulard are utilized to create a tailored mask for each perijove, identifying the regions where outer emissions are present. The data for the main oval mask were stored 1800 by 3600 pixels wide cylindrical maps, which corresponds to a spatial resolution of 0.1° in both latitude and longitude. Regions where the main emission occurs contain non-zero pixel values, while all other pixels are set to zero.

This file can also be displayed in polar view where the shape of the main emission appears irregular and asymmetrical. To identify the regions corresponding to external emissions, the areas representing the main emission, polar emission, and the Io

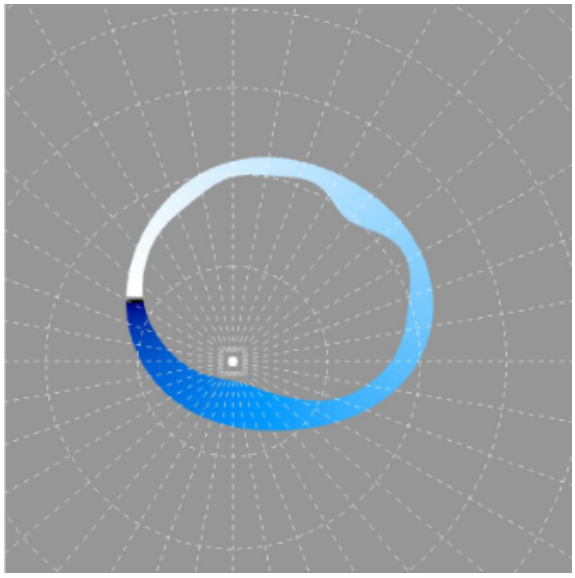

Figure 3.1 Representation of the mask, for Perijove 1 in the South Hemisphere, made by Antoine Groulard during his master thesis (Groulard et al. 2022)

footprint must be excluded. After applying a vertical transposition, all pixels whose coordinates lie inside the shape of the main emission must be set to non-zero values.

Subsequently, an inverse image is created: all pixels that are equal to 0 become 1, while all non-zero pixels are set to 0. Another image of the same dimension is then generated, representing a filled ellipse where all pixels inside the ellipse are set to 1, and those outside are set to 0. This ellipse separates the Io footprint from the external emission regions.

External emission regions are determined by combining the inverted main emission mask with the ellipse image. Results for both hemispheres during Perijove 1 are presented in Figure 3.2. To verify whether the structures detected in the previous step belong to the external emission region, their longitudes and latitudes are converted into pixel coordinates. The corresponding pixel value is extracted from the mask. If the pixel value is non-zero, the structure is indeed located within the external emission region. Conversely, if the pixel value is zero, then it does not belong to that region.

3.3 Successive spin maps

To construct the best possible light curve for each structure identified in the detection step and to determine the direction of the shift between the brightness peak and the color ratio peak, maps of each structure must be created. These maps must meet an important criterion: the time gap between the captures of successive auroral ribbons must be short enough to avoid mixing non-successive ribbons.

To handle this constraint, a routine has been developed. This procedure involves multiple steps, each applied independently to every detected blob in the outer emis-

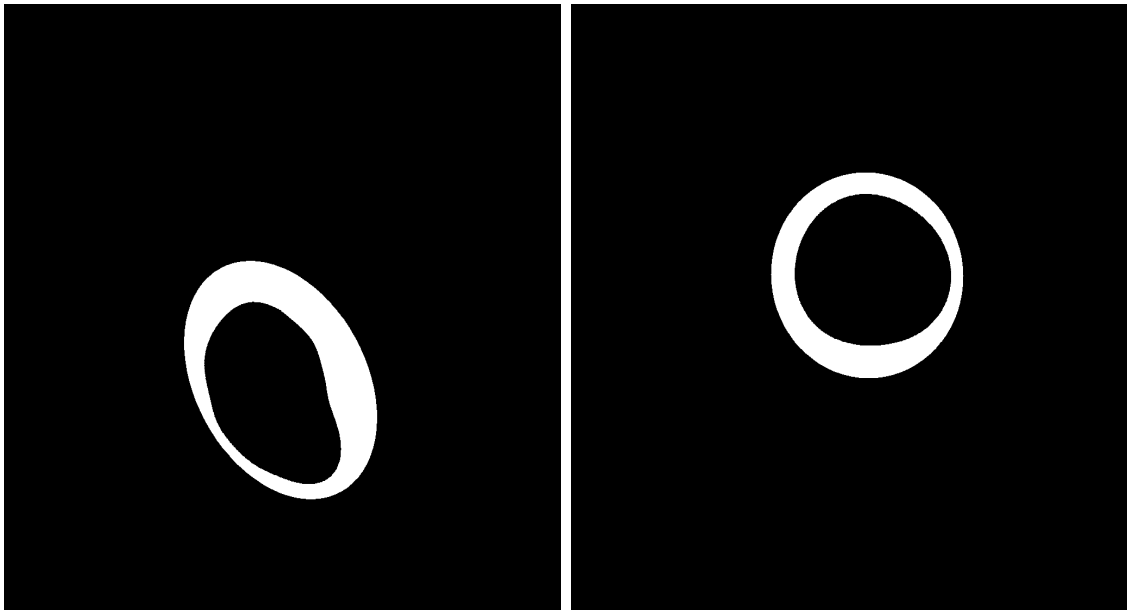

Figure 3.2 Representation of the binary mask illustrating the areas of outer emissions detected for the North (left panel) and South (right panel) Hemispheres for the first Perijove. In white the regions where the outer emission occurs and in black the others emission and the background.

sion. Creating maps that fully cover the structure of interest requires combining several auroral ribbons. To identify the files corresponding to the ribbons covering the target area, the mask files are used first. Each mask image contains three strips, which correspond to the detector's field of view. Files are organized consistently with a common base name indicating the spin and ribbon number (for example, spin1_001), followed by a suffix that denotes the data type, such as masks, detection wavelength, etc. Files sharing the same ribbon identifier (like spin1_001) cover the exact same area but contain different types of data depending on the measurement performed. This step is performed separately for each blob in every perijove. The following steps focus on one blob at a time but are repeated for each blob in the same manner.

3.3.1 Creation of an image representative of the blob

A binary image is created based on the results from the blob detection step, where the size of each structure was initially defined. This image shows a circle centered on the coordinates of the detected blob. The circle's radius is set to three times the radius of the original blob to define an enlarged area around the detected center. Pixels inside the circle are assigned a value of 1, while pixels outside are set to 0. The resulting image, illustrated in Figure 3.3, represents the target area to be covered. This image is then used as a reference to assess how well the combination of the various generated masks cover the area.

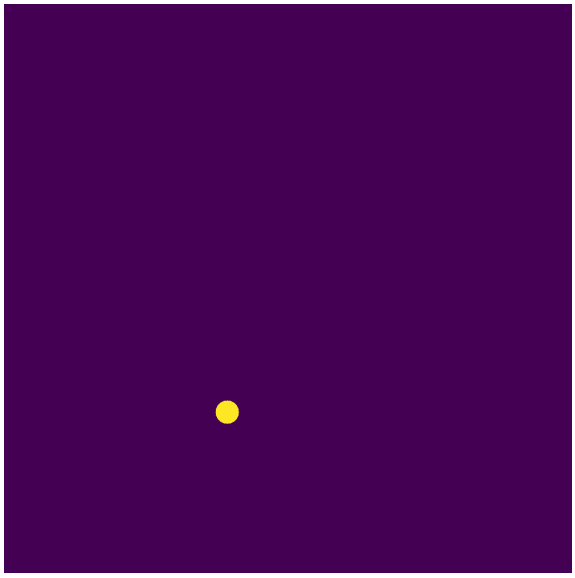

Figure 3.3 Image representative of the blob considered during perijove 8 at latitude 61° and longitude 206.30° in the Northern Hemisphere.

3.3.2 Selection of ribbons covering the blob

For this step, the masks made by Juno UVS are used. They provide information on the regions of the aurora that were observed. These mask images, shown in polar view, consist of three bands representing the different sections of the spectral slit (Figure 3.4). To fully cover the area of interest, represented by the blob image created in the previous step, multiple ribbons need to be combined. The goal of this step is to identify the filenames of the masks that cover the target area. This allows to construct the corresponding maps. Several criteria must be considered when selecting these ribbons.

First, because Juno approaches Jupiter from the north and then moves away toward the south, the spins with the best resolution for the northern aurora are those recorded last during the northern passes, while the first spins in the south provide the best resolution for the southern aurora.

Second, the ribbons selected to reconstruct the area must have been recorded within a 5-minute time interval. To respect this condition, only five consecutive ribbons are considered at once. The time difference between the first and last ribbon in this group must be less than 300 seconds. If the time interval is longer, the earliest ribbon is discarded and replaced by the next ribbon, and so on.

Third, the combined mask images must cover the area of interest sufficiently. To evaluate the quality of the coverage, each mask ribbon image is first converted into a binary image. During this conversion, only pixels with a value of 1 or 5 in the original image are retained and set to 1, while all other pixels are set to 0 (Figure 3.5. These binary images are then added together, following the criteria described above.

To quantify the quality of the overlap, the average overlap image is multiplied pixel-

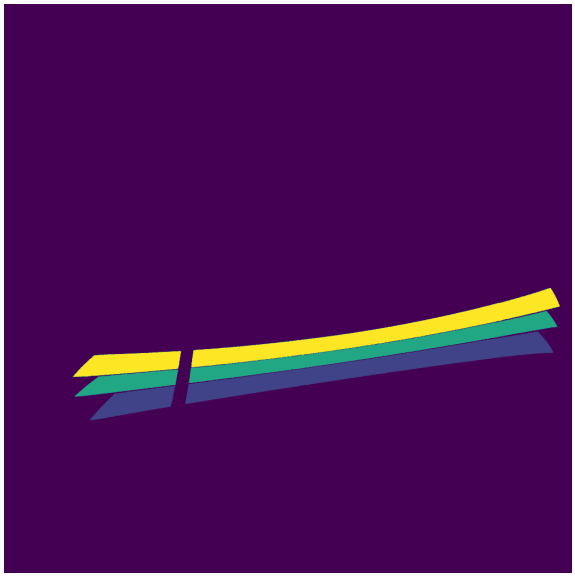

Figure 3.4 Mask obtained for the Juno observation of Perijove 8 during its 121st observation. The mask represents three bands, shown in different colors. These colors encode the different parts of the spectral slit: the left and right bands (shown here in blue and yellow) correspond to the wide slits, while the central band (green) corresponds to the narrow slit. A gap is observed in the bands. This gap is due to the saturation of the instrument's readout electronics caused by an excessively high counting rate.

by-pixel with the target blob image. This operation produces a new image, which we call the covering image in this work. In this covering image, each pixel's value is determined as follows: if the pixel value at that position is different from zero (i.e., greater than zero), it is assigned a value of 1; if the pixel value is zero, it remains 0. This process effectively creates a binary map showing which pixels of the target area are covered by the combined mask images. After this, the sum of all pixel values in this binary covering image is calculated. This sum represents the number of pixels successfully covered by the masks. To express this coverage relative to the target, the sum of covered pixels is divided by the sum of all pixel values in the original target blob image, which represents the total area of interest. This division gives a ratio between 0 and 1. Finally, to convert this ratio into a percentage, it is multiplied by 100. This percentage represents how much of the target structure is effectively covered by the masks, allowing assessment of the completeness of the coverage. Coverage is considered satisfactory when 90% or more of the target area is covered by the masks.

3.3.3 Map production

After identifying the relevant ribbons using the mask files, their identifiers are used to select the corresponding scientific data files and build the maps. The resulting images have a size of 1800 x 3600 pixels.

For the brightness calculation, files corresponding to the detection in the wavelength

Figure 3.5 Binary mask obtained for perijove 8 in the Northern Hemisphere during its 121st observation after the transformation. This is the same mask as for figure 3.4 but with values 1 and 5 replaced by 1 and the others by 0. A filter was applied to the image to enhance its visibility.

range 155-162 nm are used. The images obtained from these files will be referred to here as H_2Ly images. For each selected ribbon, the H_2Ly image is multiplied by the associated mask image, which has been converted to a binary mask. This operation extracts only the relevant pixels in each image. This step is repeated individually for all selected ribbons. Once all images are filtered by their respective masks, they are summed to create a composite image. This sum is then normalized by dividing the resulting image by the sum of the binary mask images, producing an average value weighted by the effective overlap of each ribbon. Figure 3.6 illustrates the five successive ribbons used to cover one of the structures detected in the Northern Hemisphere during Perijove 8. This structure is located at a latitude of 61° and a longitude of 206.30°, and was identified through its emission in the wavelength range 155-162 nm.

For the color ratio maps, the same data processing procedure as used for detection in the wavelength range 155-162 nm is applied to the detections in the wavelength range 125-130 nm. The images obtained from these files will be referred to here as H_2We images. For the specific structure considered here, five detection ribbons covering the same spatial regions as those used in the H_2Ly image analysis are selected from the H_2We image. These ribbons are shown in Figure 3.7. Although the spatial coverage is identical, the intensity values differ, as they are based on two distinct spectral bands. The color ratio map is then obtained by dividing the processed H_2Ly image by the processed H_2We image.

Examples of the resulting brightness map and color ratio map are presented in Figure 3.8. These maps were generated using the same set of spectral ribbons, selected to cover the auroral structure located at 61° latitude and 206.30° longitude during Perijove 8.

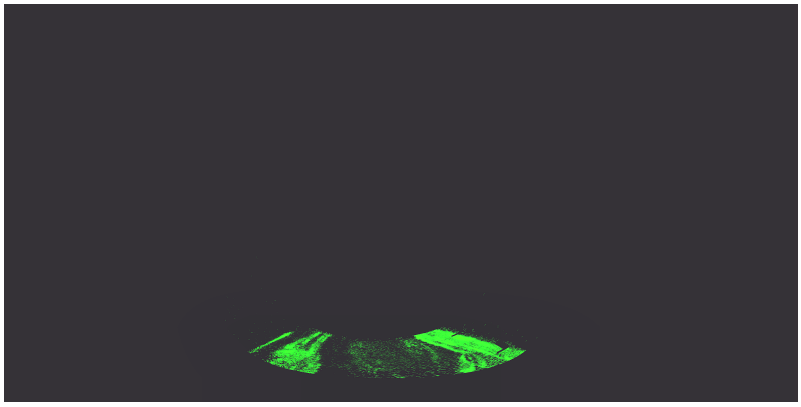

Figure 3.6 Five detection ribbons in the wavelength range 155-162 nm covering an auroral structure located at 61° latitude and 206.30° longitude in Jupiter's Northern Hemisphere during Perijove 8. These ribbons were used to generate the composite brightness and color ratio maps. Due to partial overlap, individual ribbons may not be visually distinct. A filter was applied to the image to enhance its visibility.

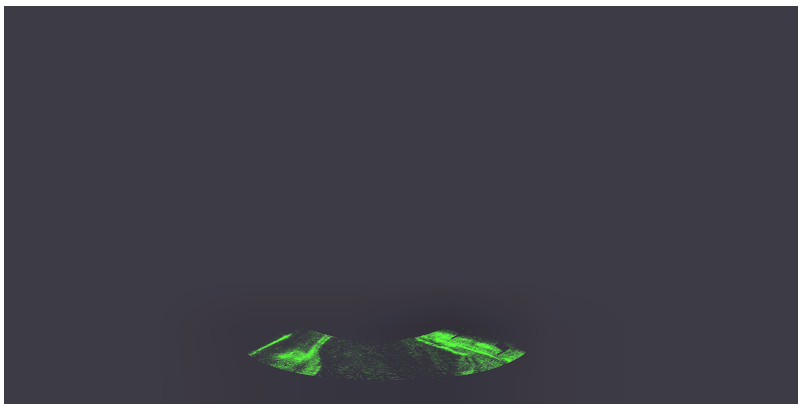

Figure 3.7 Five detection ribbons in the wavelength range 125-130 nm covering the same spatial regions as the ribbons shown in Figure 3.6, for the structure located at 61° latitude and 206.30° longitude during Perijove 8. These data are used to compute the color ratio map. A filter was applied to the image to enhance its visibility.

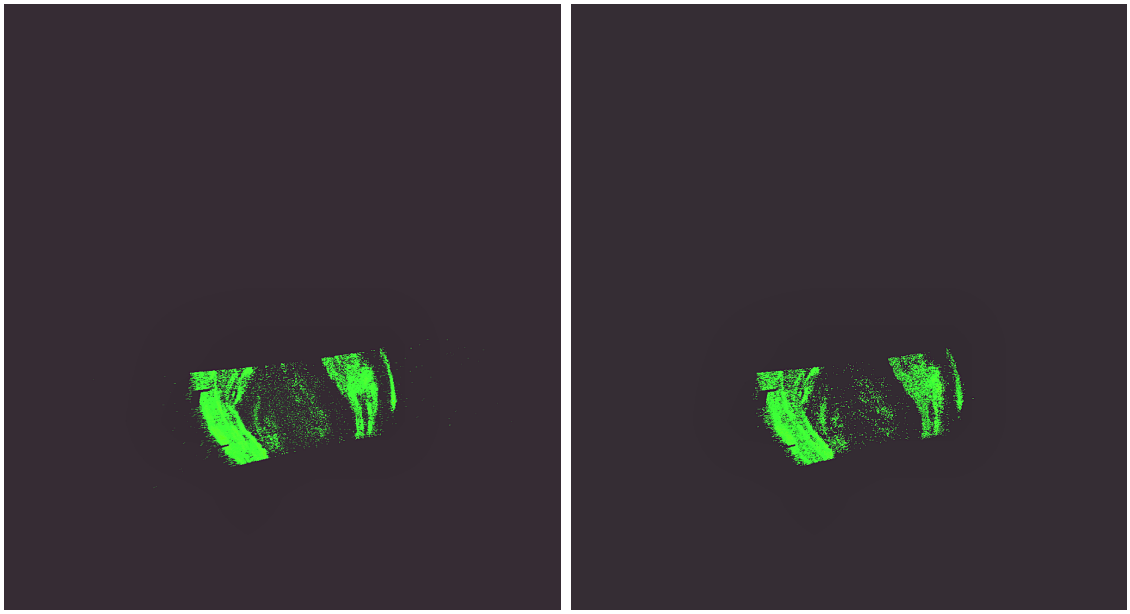

Figure 3.8 Example of a brightness map (left) and a color ratio map (right) derived from the spectral ribbons covering the auroral structure detected at 61° latitude and 206.30° longitude during Perijove 8 in the Northern Hemisphere. These maps illustrate the spatial distribution of emission intensity and the relative contribution of spectral bands, respectively in a polar view. A filter was applied to the images to enhance their visibility.

3.4 Size of the structure

The code used for structure detection provides an approximate size of each structure in pixels. This approximation is due to the detection algorithm that draws a circle around the structure to ensure the entire structure is enclosed. In other words, if the structure is elliptical or irregular in shape, the detection code still uses a circle that encompasses the whole structure and its surrounding background. As a result, the calculated area based on this circle includes not only the structure itself but also some background pixels, leading to an overestimation of the true size. Alternatively, it can exclude parts of the structure, resulting in an underestimation of its size.

Based on the coordinates provided by the detection step, a square window is extracted from the 1800 × 3600 pixel image created by combining the successive ribbons. The size of this window is set to twice the radius given by the detection step plus one pixel, ensuring the window has an odd number of pixels per side. This choice allows the structure to be centered precisely within the window. Within this window, which is centered on the initially detected coordinates, the pixel with the maximum intensity is identified. The coordinates of this intensity peak are then taken as the new reference coordinates of the structure, replacing the initial ones provided by the detection algorithm. This adjustment enhances the accuracy of the structure's position, since the detection step may not always perfectly identify the true center of brightness.

To reduce the error on the size of the structure and obtain a more accurate esti-

mation of the structure's area, an additional method was developed. This method determines the number of pixels within a shape defined by a specific intensity threshold. The approach is as follows. First, a small square region is extracted from the composite image created by summing the successive ribbons. This square is centered on the new coordinates of the structure's detected center. From this extracted region, a Boolean mask is generated to retain only pixels with intensities greater than or equal to a defined threshold. In this mask, pixels with intensities above the threshold are assigned a value of 1, and all remaining pixels are assigned a value of 0.

The intensity threshold is defined as a fraction of the intensity of the structure's center, scaled by an adjustable parameter called the alpha coefficient. This coefficient controls the strictness of pixel selection: when alpha is 0, all pixels—including noise—are included; when alpha is 1, only the single pixel with the maximum intensity is included, which is insufficient to estimate the full structure size. Thus, alpha values between 0 and 1 help isolate the meaningful parts of the structure. In this method, the intensity threshold used to define the structure is calculated as a fraction of the maximum intensity within the extracted window. This fraction is determined by a coefficient called alpha. In this work, an alpha value of 0.37 was chosen, which corresponds approximately to the point where the intensity has dropped to 1/e of its maximum value. By using this threshold, the selected pixels include the core of the structure while excluding most of the surrounding background and noise. It strikes a balance between capturing the significant extent of the auroral feature and avoiding overestimation due to low-intensity peripheral pixels. The resulting area estimation is thus more representative of the physical size of the structure.

Next, a Python function extracts the contour of the shape by detecting transitions between values below 0.1 and values above 0.1 in the Boolean mask. The threshold of 0.1 was empirically chosen to separate background noise from the real signal. If multiple contours are found, the one with the largest number of points is selected. For this reason, the extracted region must be large enough to contain the whole target structure but not so large as to include unrelated features that could confuse the contour detection.

The code may detect several contours. To ensure the correct one is selected, an additional criterion is applied: only the contour that contains the center of the window is retained. This ensures that the chosen contour corresponds to the structure of interest, rather than to unrelated features within the window. Once the appropriate contour, centered on the target structure, is identified, the area in pixels is computed by counting all pixels enclosed within this contour.

To convert the pixel area into square kilometers, an external file containing 1800 values is used. Each value corresponds to the surface area (in km^2) of a pixel at a specific latitude, sampled every 0.1° of latitude. The calculation proceeds by counting the number of pixels belonging to the structure for each latitude. The computation of the number of pixels for each latitude is done by using the contour coordinates. This calculation is performed by determining the difference between the extreme longitudes making up the blob contour for each latitude. This pixel count is then multiplied by the corresponding pixel area value from the external file

for that latitude. Finally, the total area of the structure is calculated by summing these contributions over all relevant latitudes, providing an accurate measurement in square kilometers.

3.5 Reference line

Each point constituting the reference line is used to construct the plot of the intensity as a function of the longitude by extracting the intensity at that point. This curve must be the same in the brightness and color ratio maps. The construction of this curve is done in the equatorial plane following several steps. To construct the curve in the equatorial plane, the magnetic field line related to the structure must be drawn. To represent this magnetic field line on either side of a given coordinate, a model is used (DOI: 10.5281/zenodo.6822191).

The model used in this work is the JRM33 (Connerney et al. 2022) and presents the internal magnetic field in terms of spherical harmonic expansion. This model is used together with the Con2020 model of the external (ECS) magnetic field and uses data from Juno's first 33 orbits to build a magnetic field model using spherical harmonics up to degree 30 (Wilson et al. 2023). The data were averaged over 30-second intervals and collected within 2.5 RJ of Jupiter. These 33 orbits allowed Juno to complete its planned map of Jupiter's magnetic field at 32 evenly spaced longitudes (Juno went into safe mode on approach to perijove 2). The model's coefficients were computed in the System III coordinate system, where 1 RJ is defined as 71,492 km. Using a specific command, the coordinates of each point constituting the magnetic field line can be extracted.

For each structure observed, detected and in the selected zone during each perijove, a magnetic field line is traced through the coordinates of the structure. An example of such a field line is shown in Figure 3.9.

The point where the magnetic field line intersects the equatorial plane is used as the center of a circular arc. However, not all field lines cross the equatorial plane exactly at z=0. To address this, a custom code was developed to identify the point on the field line that lies closest to the equatorial plane, with a z-coordinate restricted between -0.3 and 0.3. This nearest point is then used as the "intersection point."

Using this intersection point, a circular arc is constructed within the plane parallel to the equatorial plane. The radius of the arc is defined as the distance from the center of Jupiter to the intersection point, with the z-coordinate of the radius equal to that of the intersection point. The arc extends symmetrically in both directions from this central point (with the arc remaining in the same z-level as the intersection point).

Once the arc is constructed, it is translated to the auroral region while preserving its shape, size, and orientation. The midpoint of the arc now corresponds to the original coordinates of the observed structure.

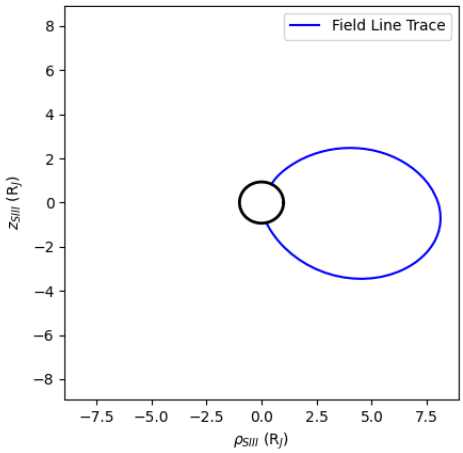

Figure 3.9 Representation of the magnetic field line drawn by the JUPITERMAG code for the blob situated at latitude 61° and longitude 206.30° during the eighth PJ in the Northern Hemisphere.

To adjust the arc of circle to the desired size, specifically ten times the radius of the structure considered, the curve was rescaled after being generated and correctly positioned. The rescaling was performed by multiplying the Cartesian coordinates of each point by a constant factor corresponding to the ratio between the target length and the initial length of the arc. This transformation preserved the angular distribution and the total number of points, ensuring that the geometry of the arc remained consistent while fitting the required spatial scale. Figure 3.10 provides a visual representation of this method, showing the polar projection from Perijove 8 in the Northern Hemisphere, with the red arc corresponding to the final, rescaled detection curve centered on the auroral structure.

The rescaled arc is then used to generate light curves for both brightness and color ratio maps. The coordinates of the translated arc serve as the reference for these analyses.

3.6 Light Curve Construction

Once the maps and reference lines have been produced, light curves for each blob can be extracted. To do this, the circular arcs defined using the methodology described in Section 2.1.1 are used. The coordinates of these arcs are initially expressed in latitude and longitude and must be converted into pixel coordinates to extract the corresponding intensity values that form the light curves.

For the master maps, the arcs are mapped onto images of 1024 × 1024 pixels, and a dedicated function is used to convert latitude/longitude coordinates into pixel positions for the maps in a polar view representation. However, this function does not apply to the successive spin maps, which are based on raw data files with a resolution of 1800 × 3600 pixels. These raw files are organized as 2D arrays with

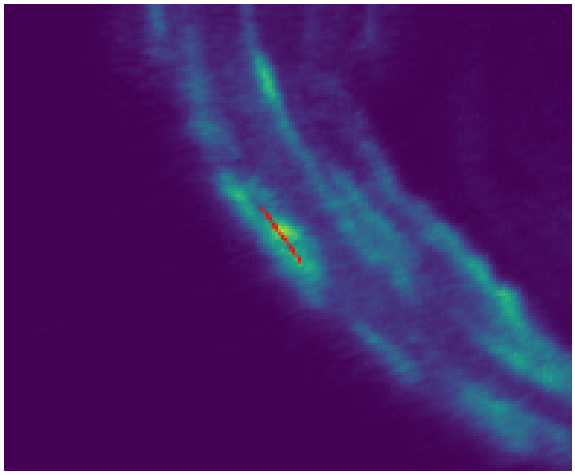

Figure 3.10 Polar projection of the auroral region observed during Perijove 8 in the Northern Hemisphere. The red curve represents the rescaled detection arc, centered on the auroral structure of interest (61° latitude and 206.30° longitude) and adjusted to a length ten times larger than the structure's radius. This arc was constructed in the equatorial plane, translated to the appropriate position, and resized to match the desired spatial scale.

latitude and longitude as the two axes.

Several tests were carried out to determine the geographic correspondence of the pixel grid. The results showed that the first pixel in these raw images corresponds to a latitude of -90° and a longitude of 0°. Based on this, a general equation can be defined to compute the pixel coordinates of any point along the arc, using its latitude and longitude.

Once the pixel coordinates of each point along the arc are determined, their intensities are extracted to construct the light curve. This is done for both brightness and color ratio data. To minimize noise and highlight the overall signal trend, two smoothing operations are applied.

In the first smoothing step, a 7×7 pixel square is defined around each point along the arc, centered on its pixel coordinates. The intensity value assigned to that point is the average of all pixel values within this square. This process is repeated for every point on the arc, producing a smoothed light curve that reduces the impact of local intensity fluctuations.

In the second smoothing step, a sliding average is applied to the resulting intensity values using a three-point window. Specifically, the first point of the final curve is computed as the average of the first three values. The window then slides forward by one point at a time: points 2–4 are averaged, then 3–5, and so on, until the end of the arc. This additional smoothing step further reduces residual noise while preserving the overall shape and trend of the light curve.

The resulting intensity profile as a function of longitude is shown in Figure 3.11. This curve corresponds to an auroral structure observed during Perijove 19 in the Northern Hemisphere.

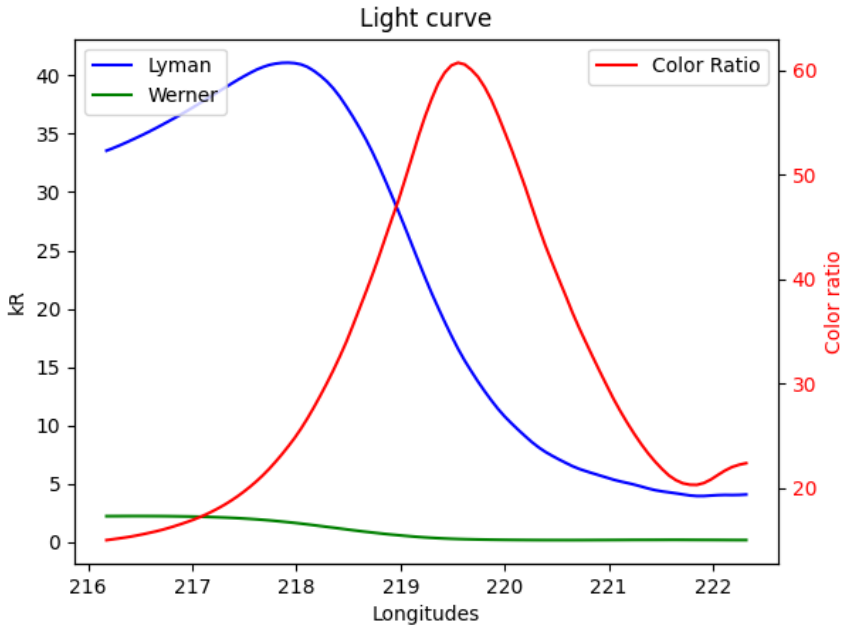

Figure 3.11 Longitude-intensity profile for an auroral structure detected during Perijove 19 in the Northern Hemisphere associated with a negative shift. The intensity values were extracted along the circular detection arc, and two levels of smoothing were applied to reduce noise and reveal the main spatial trends.

To quantify the spatial shift between the brightness peak and the color ratio peak, the longitudinal difference between the respective maxima was computed. This was done by identifying the longitude at which the brightness reaches its maximum intensity and subtracting it from the longitude corresponding to the maximum intensity in the color ratio curve. The resulting value provides a measure of the angular offset between the two profiles.

3.7 RGB maps

To investigate potential differences between the brightness peaks and the color ratio peaks, dedicated RGB (Red, Green, Blue) maps are constructed. These maps are designed to visually highlight any spatial displacement between the two types of emissions by superimposing the contributions of detections from the wavelength range 155-162 nm and 125-130 nm using different color channels.

In these RGB maps, the contribution of the wavelength range 155-162 nm contribution is displayed in red, while the color ratio is shown in green. The maps are generated using successive auroral ribbons, selected to cover at least 90% of the detected structure, ensuring reliable spatial coverage.

If the peaks of brightness (detection in the wavelength range 155-162 nm) and color ratio (ratio between detection in the wavelength 155-162 nm and 125-130 nm) coincide, the corresponding region on the RGB map will appear yellow, indicating no

spatial displacement. Conversely, if the two peaks are spatially distinct, the map will show two separate structures: one red (representing the detection in the wavelength range 155-162 nm) and one green (representing the color ratio).

These RGB maps allow for a direct visual inspection of the spatial offset between the emissions (see Figure 3.12. For each identified structure, any displacement between brightness and color ratio peaks can be readily observed by eye, making this a powerful tool for qualitative analysis.

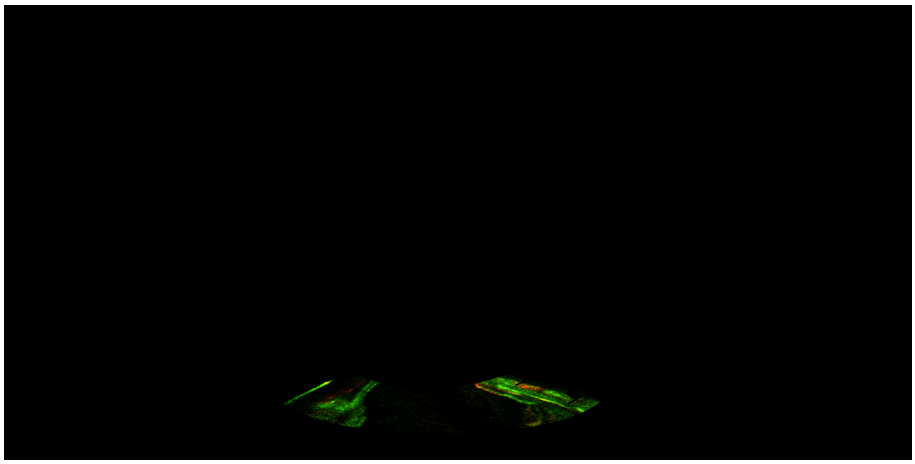

Figure 3.12 RGB composite map centered on the auroral structure detected at 61° latitude and 206.30° longitude during Perijove 8 in the Northern Hemisphere. The structure of interest is circled in green. The map was generated using the spectral ribbons selected to cover this structure, allowing for a qualitative comparison of the spatial distribution of emissions across different wavelength bands. The RGB encoding enhances the visibility of spatial offsets between components. A filter was applied to the image to enhance its visibility.

Chapter 4

Results

The detection phase resulted in the generation of several tables, each corresponding to a specific perijove and hemisphere. Each table contains all the relevant information for every detected structure, including its latitude, longitude, and length in pixels.

Among these detected structures, only 36.86 % of the structures in the Northern Hemisphere and 41,06 % in the Southern Hemisphere are associated with the external emission. The remaining structures are either linked to Io's footprint or to the main and polar emissions.

Focusing on the structures belonging to the outer emission in both the Southern and Northern Hemispheres, all structures satisfied the spatial coverage criteria. A structure is considered covered if at least 90% of its area is overlapped by five consecutive strips recorded within 300 seconds.

Among the structures that were successfully covered according to this criterion,100 % (North) and 99,68 % (South) had their sizes reliably determined using the predefined detection threshold.

Based on the analysis of the light curves, the displacements between the brightness profiles and color ratio curves were quantified. The shift of 31.43 % in the north and 31.27 % in the south for the remaining structures are not calculated because their brightness levels are low; for some structures, this was on the order of 0.001 kR. Therefore, a detection threshold was applied, excluding all detections with peak intensities below 10 kR.

Out of 1,539 detections in the south and 1,465 detections in the north, only 427 and 266 respectively could be analyzed.

After applying the methodology described in the previous two chapters, a comprehensive set of results was obtained, which are presented in this chapter.

The detected structures were categorized into two distinct groups based on their size. The first group includes structures with a surface area ranging from 31.955 to

1.115.158 km^2 referred to as small structures. The second category includes structures with surface areas ranging from 1.119.576 and 2.553.253 square kilometers, referred to as large structures.

Several statistical analyses can be carried out with those detections. Firstly, a statistical analysis of the number of blops per sector in local time and SIII position can be performed. This analysis can be used to determine whether there are any trends in plasma injections. Another statistical analysis can be introduced, looking at the disposition of small injections compared with medium and large ones.

In order to analyze the behavior of auroral structures as a function of longitude in the equatorial plane, on one hand, and local time, on the other hand, and their morphological and dynamic characteristics, statistical distributions in the form of histograms have been constructed. These allow the visualization of the distribution of detected events according to different criteria.

Histograms, as a function of the longitude in the equatorial plane, are constructed in 45-degree steps in longitude, and represent in ordinate the number of structures detected in each longitudinal interval. For the local time histograms, they are constructed in 3 hours steps in local time. Each histogram corresponds to a specific category of structure or type of behavior.

Several types of analysis are possible, depending on the criteria chosen:

- Size distribution: structures can be separated into two groups, e.g. small and large structures, according to a defined threshold. For each group, the distribution of structures is then plotted against longitude.
- Shift distribution: structures are classified here according to the sign of their shift
- Cross-analysis: it is also possible to combine the two previous criteria. For example:
  - Consider only small structures, and analyze their displacement distribution by longitude.
  - Consider only structures with zero displacement, and examine their size distribution by longitude.
  - Analyze only large structures with negative displacement, etc.

The different analyses presented above can also be performed as a function of local time and radial distance. To determine the local time of each structure, it is necessary to know the solar longitude (long_sun) measured from 0° SIII longitude to the local noon at which each band was detected. In addition to this longitude, the equatorial plane longitude (long_eq) of each structure must be known. The local time is computed using the following relation:

$$\text{local\_time} = \left(12 - \frac{\left(\text{long}_{eq} - \text{long}_{sun}\right)}{15}\right) \%24 \tag{4.1}$$

The radial distance of each detected structure was calculated from the Cartesian coordinates of points in the equatorial plane. These points were obtained by tracing the magnetic field lines passing through the structure, starting from its Cartesian coordinates on the aurora, using JRM33 model, as described in Section 3.5.

The cross-distribution approach enables to break down the population of auroral structures in detail, and better understand the links between their morphology, the shift and spatial location. It can also reveal preferential behavior according to longitude or differences between populations.

To perform this analysis, it is necessary to classify the data into size-based categories. Several approaches can be used to define these categories, depending on the structure and distribution of the dataset.

One common approach is based on quantiles, such as tertiles, quartiles, or percentiles. These methods involve sorting the data and dividing it into equal-sized portions based on rank. While easy to implement, they do not account for the actual values of the data, only their relative position. This means that values that are numerically very close can end up in different categories, which may not reflect meaningful differences.

Another approach relies on statistical measures such as the mean and standard deviation. This method considers how far each value deviates from the average. It allows for the identification of typical, unusually small, or unusually large values. However, it assumes the data is symmetrically distributed and can be heavily influenced by outliers, which may distort the classification if the distribution is skewed.

A more flexible method is clustering, such as the K-means algorithm. This is an unsupervised learning technique that groups data into clusters based on similarity, minimizing the distance between each data point and the center of its cluster. Unlike the previous methods, clustering does not rely on predefined thresholds or assumptions about the distribution. It adapts to the actual shape of the data and can discover natural groupings, regardless of their size or number.

In view of the advantages and limitations of the different techniques, the clustering approach was selected for this study. This method offers greater adaptability to the structure of the dataset and allows for a more meaningful classification based on the actual distribution of values, rather than relying on fixed thresholds or arbitrary divisions.

Subsequently, statistical distributions of both displacement types and structure sizes were constructed. These distributions were evaluated as functions of both longitude, local time and radial distance separately for the Northern and Southern Hemispheres. For each distribution, a chi-square test was performed based on the mean value. The purpose of this test is to assess whether the observed distribution of counts is consistent with the expected mean under a null hypothesis. Specifically, the null hypothesis assumes that the counts are uniformly distributed according to the expected mean, while the alternative hypothesis posits that the observed counts deviate significantly from this uniform distribution. For each test, the p-value is cal-

culated, which quantifies the probability of observing a deviation, assuming the null hypothesis is true. A high p-value indicates that the observed distribution is consistent with uniformity, whereas a low p-value suggests a significant deviation from uniformity. In the following sections, the p-value for each histogram is discussed to assess whether the detected structures are uniformly distributed or exhibit significant variations.

4.1 Longitudes

As a first step, the distribution of structure characteristics as a function of longitude in the equatorial plane are analyzed. This enables to determine whether specific longitudes are associated with preferred displacement directions, or whether structural size correlates with longitudinal position.

4.1.1 Global histogram

The results begin with a global overview of the detected structures, focusing independently on displacement and size. For each parameter, distributions are presented separately for the Northern and Southern Hemispheres. A total of four histograms are shown in this section: two related to displacement types (one per hemisphere) and two related to structure sizes (also one per hemisphere). Only structures associated with the external emission are considered in this analysis.

The distribution of detected structures across longitude in the equatorial plane reveals marked spatial variability in both hemispheres, as shown in Figure 4.1 (left panel for the Northern Hemisphere and right panel for the Southern hemisphere), highlighting the different shifts. The presence of distinct peaks in the histograms for both the Northern and Southern Hemispheres, together with statistically significant deviations from uniformity (χ^2 test, $p < 0.01$ for the Northern hemisphere and $p = 0.01$ for the Southern Hemisphere), indicates that the external emission is not evenly distributed across longitude. In the Northern Hemisphere, a higher concentration of events is observed between the range 45° - 90° and 270° - 360°. The minimum is seen between 135° and 225°. In the Southern Hemisphere, the distribution shows a different pattern with lower count observed around 90°-225°. A higher concentration of events is observed between 225° and 45°.

Regarding displacement types, the no shifts dominate in the Northern Hemispheres, particularly within the 45° – 90° longitude range. Negative and positive displacements occur less frequently, with a higher concentration of negative shifts within the 270° to 315° range. In the Southern Hemisphere, shift are similarly dominated by the no shifts, with notable concentrations between 0° and 45°. Negative and positive displacements are also less frequent in this hemisphere, but they are more evenly distributed across all longitudes

The second histogram (Figure 4.2) shows the number of events as a function of

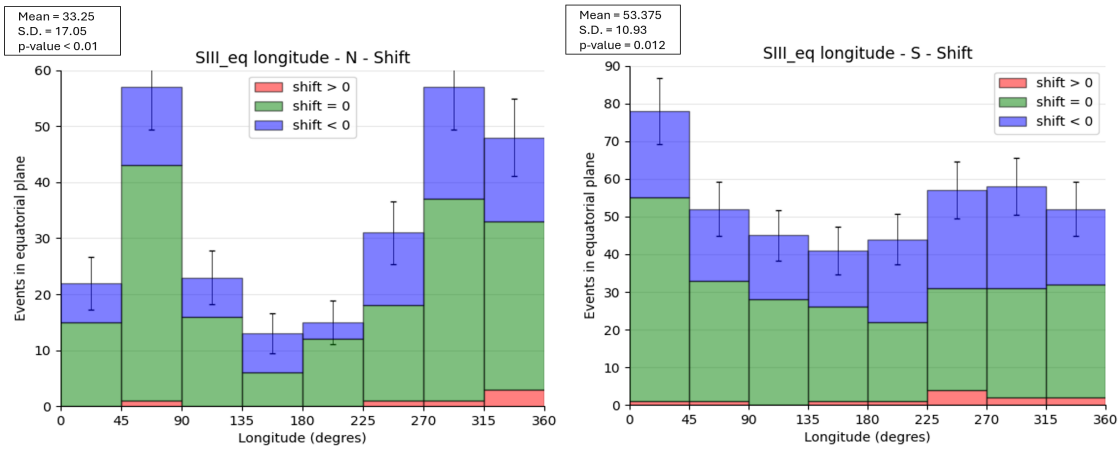

c

Figure 4.1 Histogram showing the number of detected events in the Northern Hemisphere (left panel) and in the Southern Hemisphere (right panel) as a function of ionospheric longitude SIII. The events are categorized according to their displacement direction (shift), represented by different colors: negative, zero, and positive. Bin width is 45 degrees. Only structures associated with the external emission are included. The error bars represent the statistical uncertainty on the number of events in each bin, calculated as the square root of the event counts, following the Poisson distribution. For each histogram, the mean and standard deviation (S.D.) are calculated and indicated for the corresponding distribution. A chi-square (χ^2) test is performed for each distribution, and the corresponding p-value is reported.

longitude in the equatorial plane, classified according to the size of the structure into two categories, small and large, as previously defined.

Small structures are more numerous in both hemispheres, representing 59.77 % of the detected events in the Northern Hemisphere and 74.24 % in the Southern Hemisphere. Large structures account for the remaining 40.23 % and 25.76 %, respectively.

This size distribution highlights the predominance of small-scale features within the external emission dataset. Further analysis of the interaction between structure size and displacement type is addressed in the following section.

4.1.2 Small structures

This section presents the displacement characteristics of small structures as a function of the longitudes in the equatorial plane in the Northern and Southern Hemispheres. Detailed histograms and analyses illustrate the distribution of longitudinal shifts and spatial patterns observed in these smaller-scale phenomena.

In the Northern Hemisphere, the combined distribution deviates from uniformity (χ^2 test, p-value < 0.01) (Figure 4.3, top left), exhibiting higher detection peak in the 45° - 90° and 270° - 315° ranges, while few events are observed between 135° and 180°. A significantly higher proportion of no shifts compared to other types of

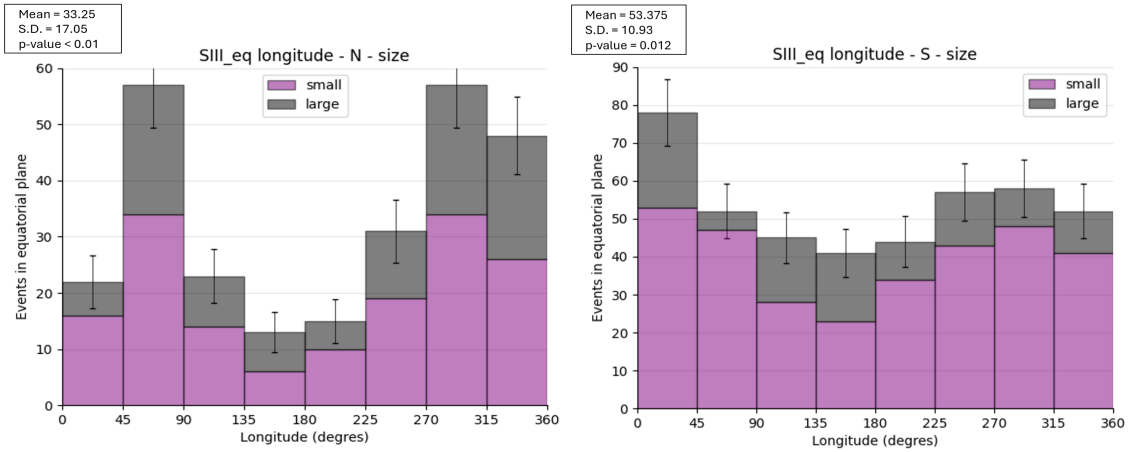

Figure 4.2 Histogram showing the number of detected events in the Northern Hemisphere (left panel) and in the Southern Hemisphere (right panel) as a function of ionospheric longitude SIII. The events are categorized according to their sizes, represented by different colors: small and large. Bin width is 45 degrees. Only structures associated with the external emission are included. The error bars represent the statistical uncertainty on the number of events in each bin, calculated as the square root of the event counts, following the Poisson distribution.For each histogram, the mean and standard deviation (S.D.) are calculated and indicated for the corresponding distribution. A chi-square (χ^2) test is performed for each distribution, and the corresponding p-value is reported.

displacements is observed. Furthermore, the spatial distribution of these structures characterized by a no shift deviates from uniformity (Figure 4.3, bottom left), as confirmed by a statistical test yielding a p-value below 0.01. Although positive shifts represent only 0.629 % of the total, a statistical test shows a p-value greater than 0.05 which means that their distribution does not significantly deviate from uniformity (Figure 4.3, bottom right). The distribution of structures with a negative shift, is non-uniform, with a statistical test indicating a p-value below 0.05 (Figure 4.3, top right).

The combined data in the Southern Hemisphere (Figure 4.4, top left), similarly to the Northern Hemisphere, reject the hypothesis of a uniform distribution at the 1 % significance level (p-value < 0.01). There is a higher concentration of events between 225° and 90°, and a lower concentration between 90° and 180°. The distribution is mainly due to structure with no shift, which also show a statistically significant departure from uniformity (4.4, bottom left). The χ^2 test on the distribution of structure characterized with a negative shift (Figure 4.4, top right) shows a p-value higher than 0.05. Positive shifts, which represent only 2.84 %, are relatively rare, and the statistical test shows, similarly to the structure with a negative shift, a p-value greater than 0.05, indicating that their distribution does not significantly deviate from uniformity (Figure 4.4, bottom right).

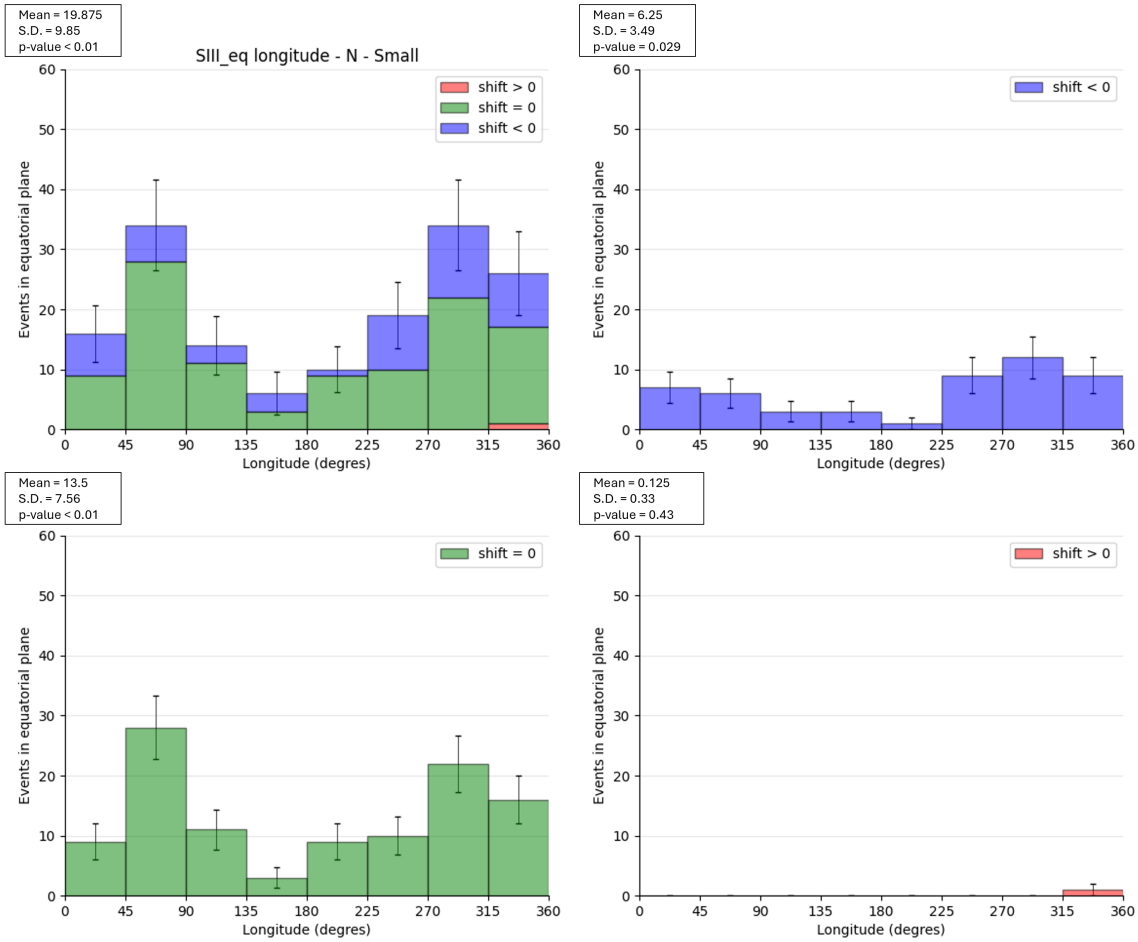

Figure 4.3 Histogram showing the distribution of small structures as a function of ionospheric longitude SIII in the Northern Hemisphere, with three different shifts combined (top left), negative shifts (top right), no-shift (bottom left) and positive shift (bottom right). Bin width is 45 degrees. The error bars represent the statistical uncertainty on the number of events in each bin, calculated as the square root of the event counts, following the Poisson distribution.For each histogram, the mean and standard deviation (S.D.) are calculated and indicated for the corresponding distribution. A chi-square (χ^2) test is performed for each distribution, and the corresponding p-value is reported.

4.1.3 Large structures

Here, the displacement behavior of large structures is examined with respect to the longitude in the equatorial plane. Comparing these results with those of small structures helps highlight size-dependent spatial trends.

In the Northern Hemisphere, evidence suggests that the distribution of the three different types of shift is not uniform at the 1 % significance level (Figure 4.5, top left). As with the distribution of small structures in the Northern Hemisphere, the highest concentration of detected structures is found in the 45° - 90° and 270° - 360° range. Only a small number of large structure were observed in the ranges 0°–45° and 180° – 225°. The proportion of structures linked to a negative shift is

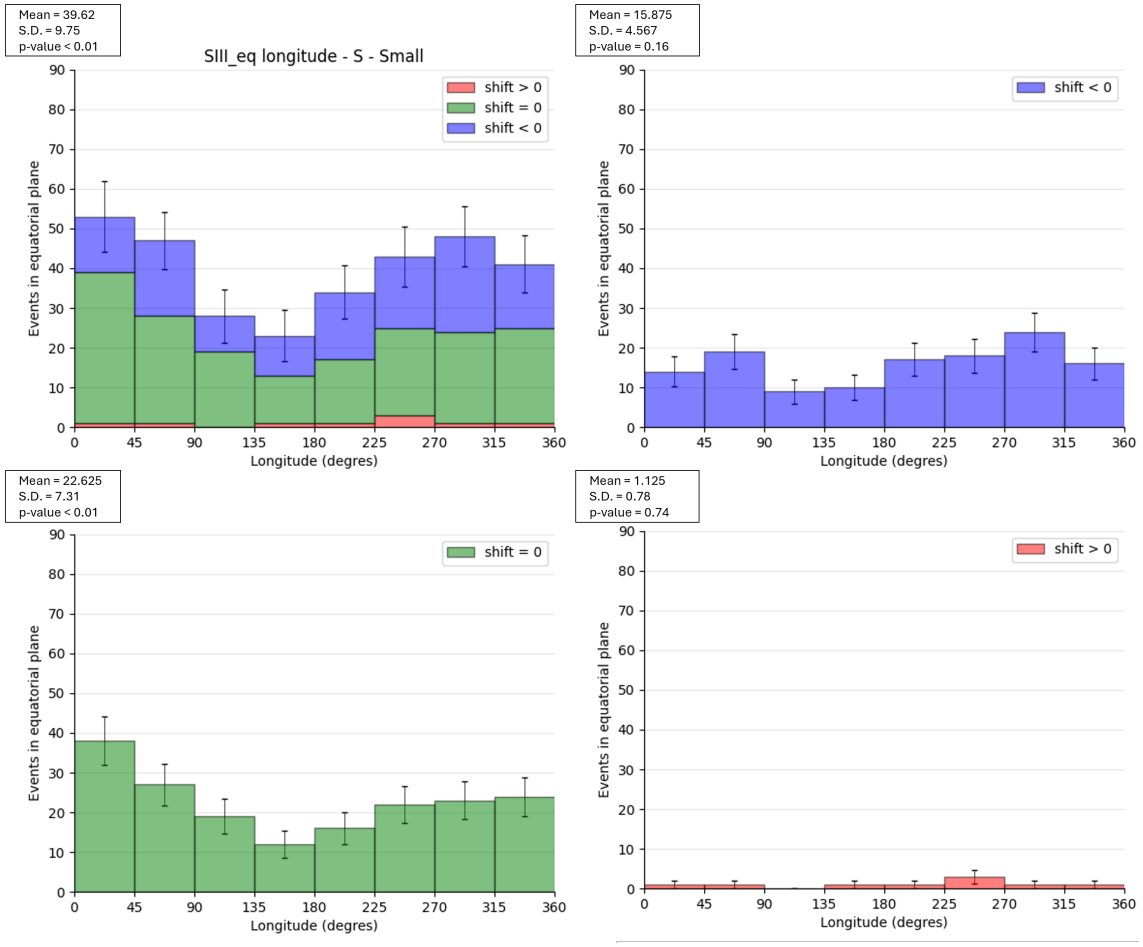

Figure 4.4 Histogram showing the distribution of small structures as a function of ionospheric longitude SIII in the Southern Hemisphere,with three different shifts combined (top left), negative shifts (top right), no-shift (bottom left) and positive shift (bottom right). Bin width is 45 degrees. The error bars represent the statistical uncertainty on the number of events in each bin, calculated as the square root of the event counts, following the Poisson distribution.For each histogram, the mean and standard deviation (S.D.) are calculated and indicated for the corresponding distribution. A chi-square (χ^2) test is performed for each distribution, and the corresponding p-value is reported.

33.64%, compared to 60.75 % for those associated with a no shift. The distributions of those two types of shit can be seen in the Figure 4.5, respectively top right and bottom left. The distribution of structures with no shift present a p-value < 0.01 which means that there is a considerable non uniformity in this distribution. For the distribution of structures with a positive shift (Figure 4.5, bottom right) and with a negative shift (Figure 4.5, top right), there is no sufficient evidence to reject the null hypothesis of uniformity (χ^2 test, p-value > 0.05).

The χ^2 test indicates that the distribution of large structure of the combination of the different shifts, in the Southern Hemisphere, is not uniform (Figure 4.6, top left). The number of events detected with a no shift is similar to that of structure with negative shift. 2.72 % of the detected structures in the Southern Hemisphere are linked to a positive shift. No significant departure from uniformity is observed

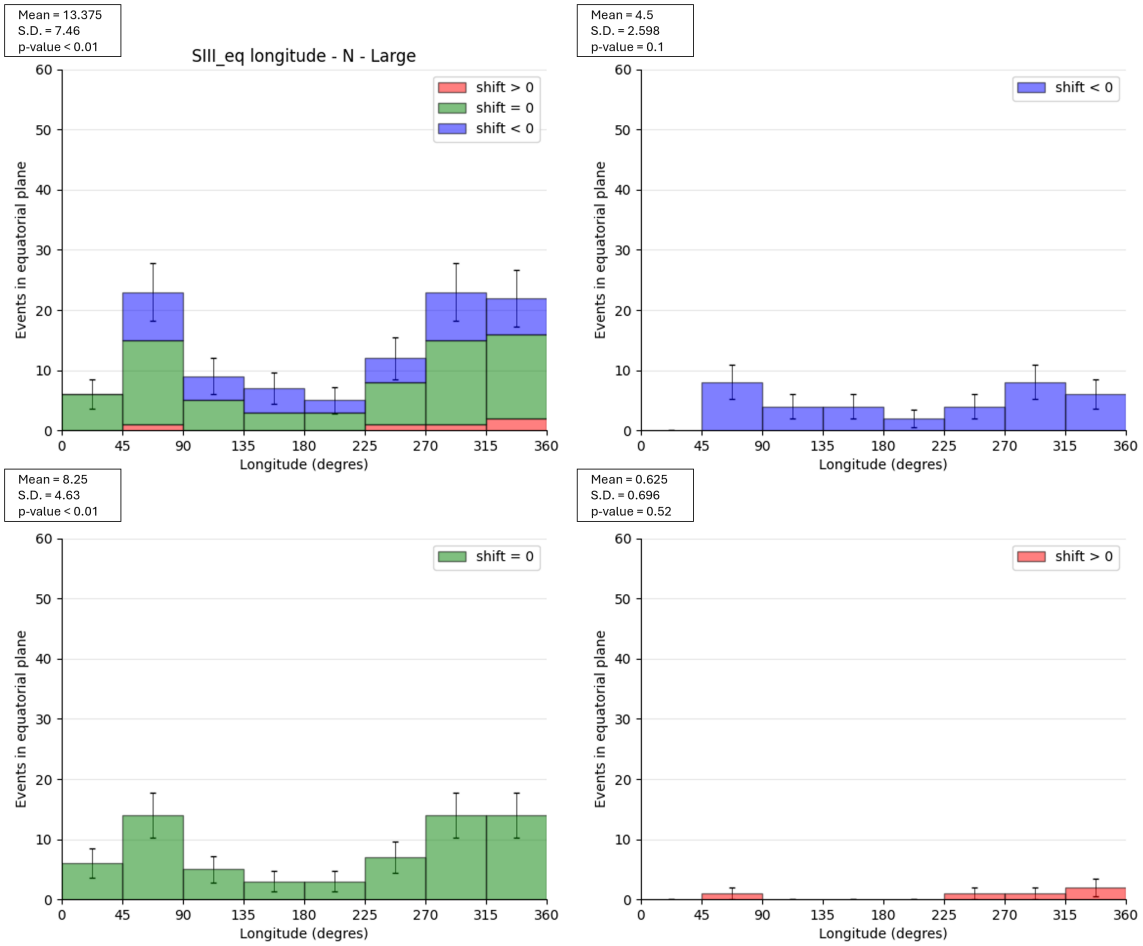

Figure 4.5 Histogram showing the distribution of large structures as a function of ionospheric longitude SIII in the Northern Hemisphere,with three different shifts combined (top left), negative shifts (top right), no-shift (bottom left) and positive shift (bottom right). Bin width is 45 degrees. The error bars represent the statistical uncertainty on the number of events in each bin, calculated as the square root of the event counts, following the Poisson distribution.For each histogram, the mean and standard deviation (S.D.) are calculated and indicated for the corresponding distribution. A chi-square (χ^2) test is performed for each distribution, and the corresponding p-value is reported.

(χ^2 test, p-value > 0.05 for the distribution of these structures (Figure 4.6, bottom right). The uniformity of the distribution of the structure with a negative shift (Figure 4.6 top right) shows similar behavior than the distribution of the structure with a positive shift. The distributions of structures associated with no shift (Figure 4.6 bottom left) does not agree with the hypothesis of a uniform distribution at the 5% significance level (χ^2 test, p-value < 0.05).

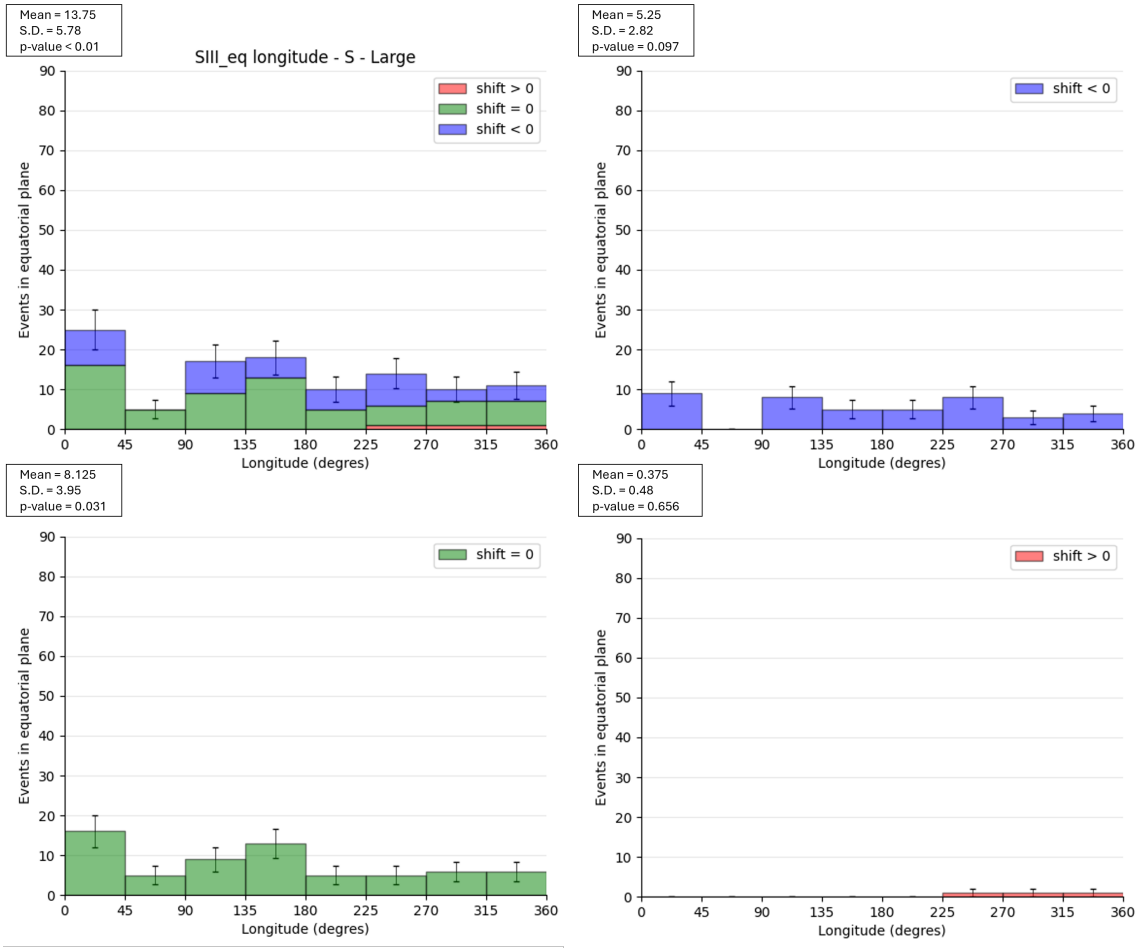

Figure 4.6 Histogram showing the distribution of large structures as a function of ionospheric longitude SIII in the Southern Hemisphere,with three different shifts combined (top left), negative shifts (top right), no-shift (bottom left) and positive shift (bottom right). Bin width is 45 degrees. The error bars represent the statistical uncertainty on the number of events in each bin, calculated as the square root of the event counts, following the Poisson distribution.For each histogram, the mean and standard deviation (S.D.) are calculated and indicated for the corresponding distribution. A chi-square (χ^2) test is performed for each distribution, and the corresponding p-value is reported.

4.2 Local time

To complement the longitudinal analysis, the variation in the distribution of structure displacements and sizes as a function of local time is examined. This approach enables the assessment of potential diurnal variations or asymmetries in the emission processes.

4.2.1 Global histogram

As for the longitude analysis, this part provides an overview of the detected structures. Four histograms are presented here as well : two for the Northern Hemisphere and two for the Southern Hemisphere, each pair including one distribution related to structure size and one related to displacement. Only structures associated with outer emissions are considered in this analysis as well.

Figure 4.7 and 4.8 show the local time distribution of detected structures, revealing pronounced spatial variability in both hemispheres (Northern Hemisphere on the left, Southern Hemisphere on the right) and emphasizing the distinct shift and the size of the structure respectively. In the Southern Hemisphere, the distribution significantly depart from uniformity (χ^2 test, p-value < 0.01). In the Northern Hemisphere, χ^2 test indicates a p-value < 0.05 meaning a significant non uniformity in the distribution. In this hemisphere, the events are more frequent between 15:00 and 24:00 LT and less frequent between 00:00 and 15:00 LT. In the Southern Hemisphere, higher concentration occur between 12:00 and 03:00 LT, whereas the 03:00 – 12:00 LT interval corresponds to a lower occurrence rate.

Examination of the displacement histograms (Figure 4.7) indicates that no shifts occur most frequently, with a higher number of events in the same intervals as those noted above. Positive shifts are relatively rare, particularly between 03:00 and 09:00 LT in the Southern Hemispheres and in the 12:00 – 15:00 and 18:00 - 03:00 intervals in the Northern Hemisphere.

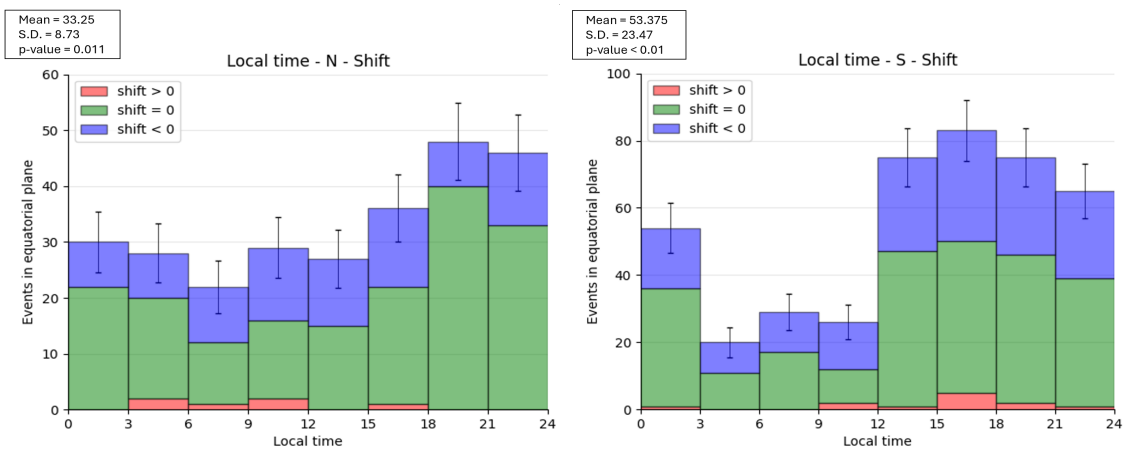

Figure 4.7 Histogram showing the number of detected events in the Northern Hemisphere (left) and in the Southern Hemisphere (right) as a function of local time. The events are categorized according to their displacement direction (shift), represented by different colors: negative, zero, and positive. Bin width is 3 hours. Only structures associated with the external emission are included. The error bars represent the statistical uncertainty on the number of events in each bin, calculated as the square root of the event counts, following the Poisson distribution.For each histogram, the mean and standard deviation (S.D.) are calculated and indicated for the corresponding distribution. A chi-square (χ^2) test is performed for each distribution, and the corresponding p-value is reported.

Focusing on the size histograms (Figure 4.8 shows that small structures are the most frequent. The difference between the small and large structures is more obvious in the Southern Hemisphere than in the Northern. In the first hemisphere, the higher concentration of small structures is between 12:00 and 03:00 LT and the lower one in the 03:00 – 12:00 LT interval. In the Southern Hemisphere, the number of small-sized events shows greater variability than in the Northern Hemisphere. In contrast, for large structures, the variation in event counts is higher in the Northern Hemisphere.

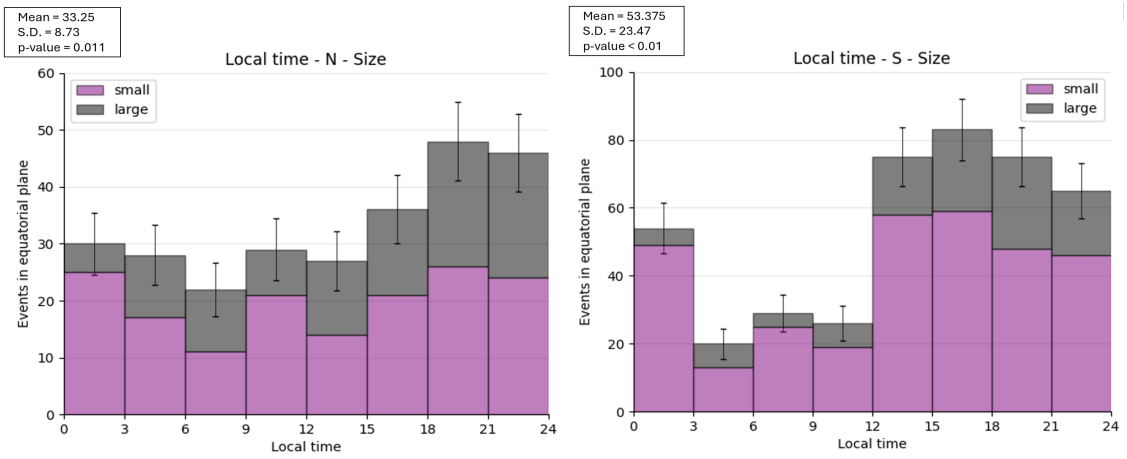

Figure 4.8 Histogram showing the number of detected events in the Northern Hemisphere (left) and in the Southern Hemisphere (right) as a function of local time. The events are categorized according to their displacement direction (shift), represented by different colors: negative, zero, and positive. Bin width is 3 hours. Only structures associated with the external emission are included. The error bars represent the statistical uncertainty on the number of events in each bin, calculated as the square root of the event counts, following the Poisson distribution.For each histogram, the mean and standard deviation (S.D.) are calculated and indicated for the corresponding distribution. A chi-square (χ^2) test is performed for each distribution, and the corresponding p-value is reported.

4.2.2 Small structures

Small structures are studied as a function of local time in this section. This enables identification of diurnal variations or temporal asymmetries in their displacement and occurrence.

In the Northern Hemisphere, the histogram with the combined shift can be seen in Figure 4.9. This distribution yields a p-value higher than 0.05, indicating that the observed result is not statistically significant and that the null hypothesis is not rejected. A mean of 19.875 events was detected per 03:00 LT bin, with a higher proportion of structures associated with zero shifts. A chi-square test on the distribution of all structures, considering each type of shift independently, shows no significant deviation from the mean. These distributions, along with their associated

p-values, are presented in figure 4.9 (top right, bottom left and bottom right panels correspond to structures related to negative shifts, no shifts and positive shifts respectively).

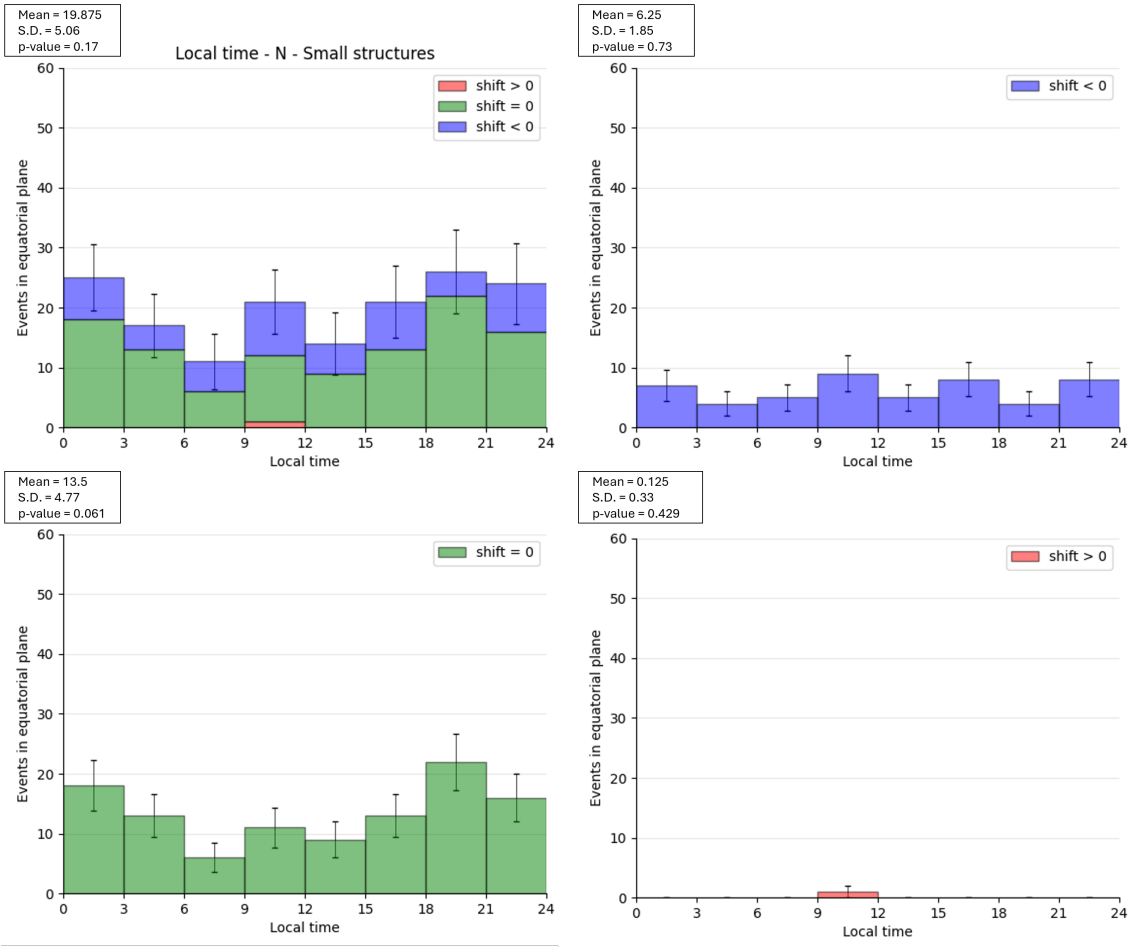

Figure 4.9 Histogram showing the distribution of small structures as a function of local time in the Northern Hemisphere, with three different shifts combined (top left), negative shifts (top right), no-shift (bottom left) and positive shift (bottom right). Bin width is 3 hours. The error bars represent the statistical uncertainty on the number of events in each bin, calculated as the square root of the event counts, following the Poisson distribution.For each histogram, the mean and standard deviation (S.D.) are calculated and indicated for the corresponding distribution. A chi-square (χ^2) test is performed for each distribution, and the corresponding p-value is reported.

Unlike in the Northern Hemisphere, the combined distribution of shifts in the Southern Hemisphere shows a p-value below 0.01, indicating a distribution not uniform (Figure 4.10, top left). A higher concentration of events is observed between 12:00 and 03:00 LT, with fewer events occurring between 03:00 and 12:00 LT. The proportion of events with no shift is higher than that of structures exhibiting negative shifts. Both distributions of small structures characterized by negative shifts and no shifts (Figure 4.10 top right and bottom left respectively) provide evidence against the null hypothesis of uniformity (χ^2 test, p-value < 0.01). The number of events detected with a positive shift is very small, with a mean of 1.125 (Figure 4.10, bottom

right). This distribution is consistent with uniformity (p-value > 0.05).

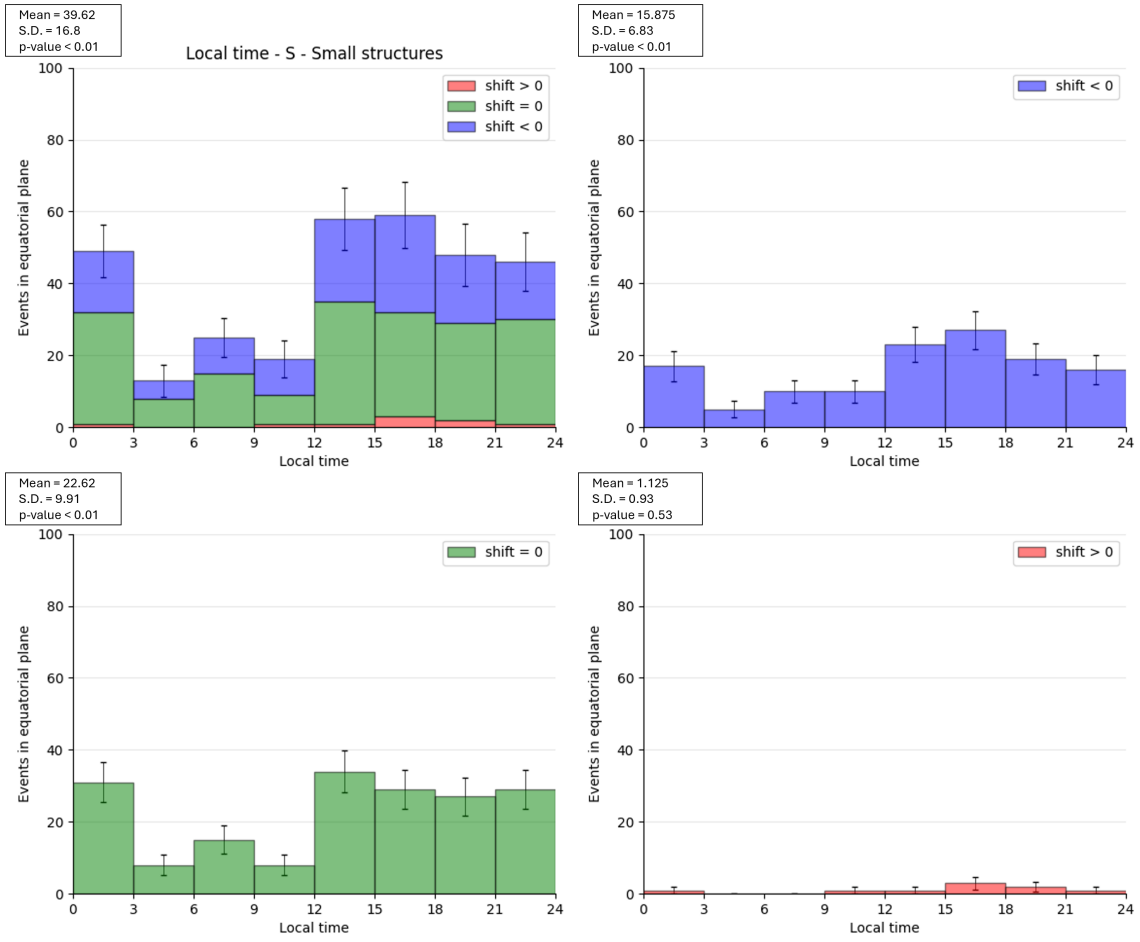

Figure 4.10 Histogram showing the distribution of small structures as a function of local time in the Southern Hemisphere, with three different shifts combined (top left), negative shifts (top right), no-shift (bottom left) and positive shift (bottom right). Bin width is 3 hours. The error bars represent the statistical uncertainty on the number of events in each bin, calculated as the square root of the event counts, following the Poisson distribution.For each histogram, the mean and standard deviation (S.D.) are calculated and indicated for the corresponding distribution. A chi-square (χ^2) test is performed for each distribution, and the corresponding p-value is reported.

4.2.3 Large structures

Finally, large structures are analyzed according to local time to determine whether they exhibit distinct temporal patterns, complementing the findings from smaller structures.

Large structures are not uniformly distributed in the Northern Hemisphere (χ^2 test, p-value < 0.01). There is a higher number of events in the 21:00 – 24:00 LT interval, with a larger number of no-shift structures in this interval and more negative shifts

between 12:00 – 15:00 LT (Figure 4.11, top left). The χ^2 test on the independent distributions of negative and positive shifts indicates no significant deviation from uniformity (p-value > 0.05) (Figure 4.11, top right and bottom right, respectively). The number of events where the difference between the brightness peak and the color ratio peak is positive is higher than that of small structures in the same hemisphere. The data related to the structure with no shift reject the hypothesis of a uniform distribution at the 1% significance level (Figure 4.11, bottom right).

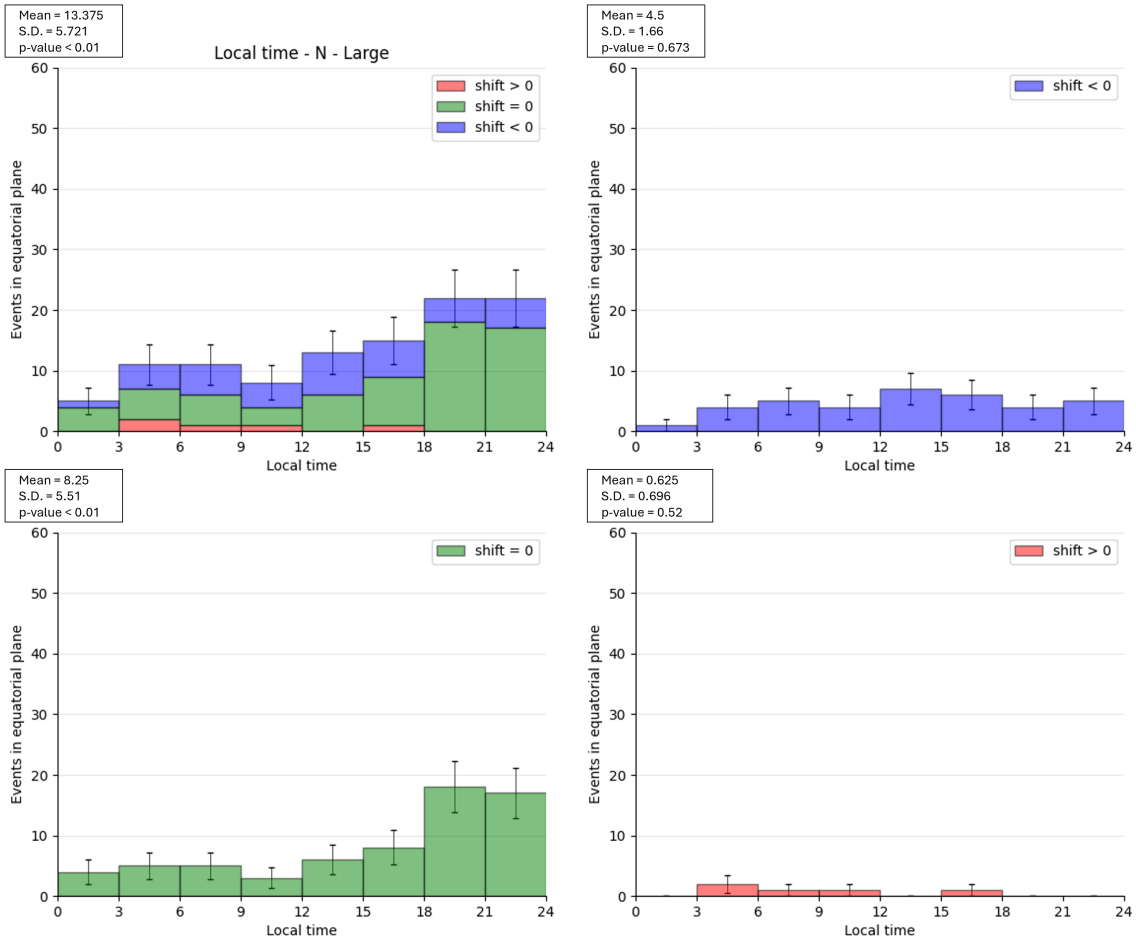

Figure 4.11 Histogram showing the distribution of large structures as a function of local time in the Northern Hemisphere, with three different shifts combined (top left), negative shifts (top right), no-shift (bottom left) and positive shift (bottom right). Bin width is 3 hours LT. The error bars represent the statistical uncertainty on the number of events in each bin, calculated as the square root of the event counts, following the Poisson distribution.For each histogram, the mean and standard deviation (S.D.) are calculated and indicated for the corresponding distribution. A chi-square (χ^2) test is performed for each distribution, and the corresponding p-value is reported.

In the Southern Hemisphere, the distribution of the large structures provides evidence against the null hypothesis of uniformity (Figure 4.12, top right) and a mean of 13.75 structures per 3-hour interval, which is similar to what was observed in the Northern Hemisphere. The 12:00 – 24:00 LT interval indicates a higher number of events. Similarly to the Northern Hemisphere, the distribution of no-shift events in

the South is not uniform ((χ^2 test, p-value < 0.01), while the distribution of positive shifts is consistent with uniformity (χ^2 test, p-value > 0.05). However, unlike in the North where the distribution of negative shifts does not reject the null hypothesis of uniformity, the Southern Hemisphere shows a distribution of these structures that rejects the null hypothesis of uniformity with moderate confidence (χ^2 test, p-value < 0.05). The distributions of large structures as a function of local time according to the shift type in the Southern Hemisphere can be found in Figure 4.12, where negative shifts are shown in the top right, no shifts in the bottom left, and positive shifts in the bottom right.

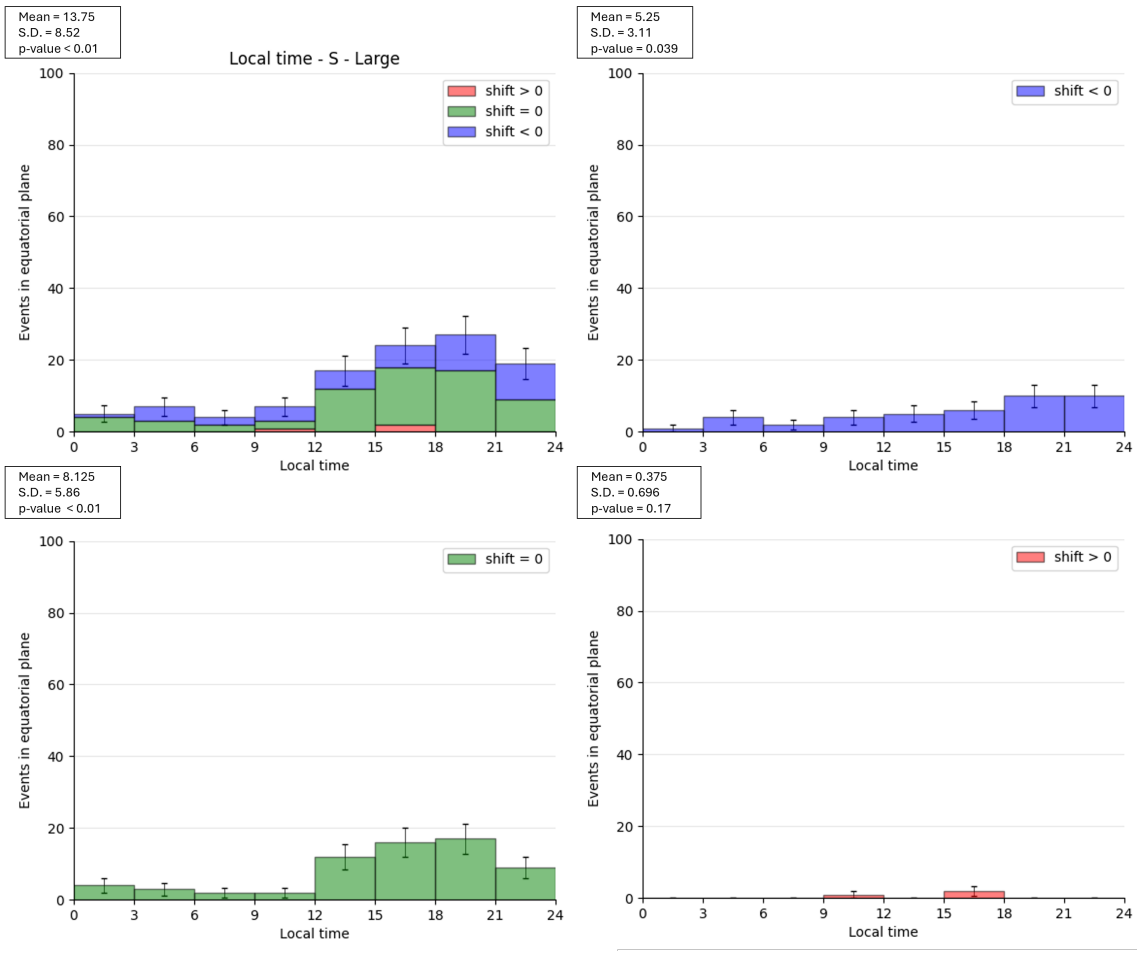

Figure 4.12 Histogram showing the distribution of large structures as a function of local time in the Northern Hemisphere,with three different shifts combined (top left), negative shifts (top right), no-shift (bottom left) and positive shift (bottom right). Bin width is 3 hours LT. The error bars represent the statistical uncertainty on the number of events in each bin, calculated as the square root of the event counts, following the Poisson distribution.For each histogram, the mean and standard deviation (S.D.) are calculated and indicated for the corresponding distribution. A chi-square (χ^2) test is performed for each distribution, and the corresponding p-value is reported.

4.3 Radial distance

Radial distributions of auroral structures in the equatorial plane were derived from data resampled into 1 RJ intervals. In the descriptions that follow, values are reported as the number of structures per RJ.

The distribution of detected events as a function of radial distance, can be found in Figure for the Northern Hemisphere and in Figure for the Southern Hemisphere.

In the Northern Hemisphere, the majority of the distribution over the radial distance is detected between 7 RJ and 16 RJ. Structures associated with no shift are more numerous between 13 RJ and 14 RJ. This interval extends down to 12 RJ for structures characterized by a negative shift.

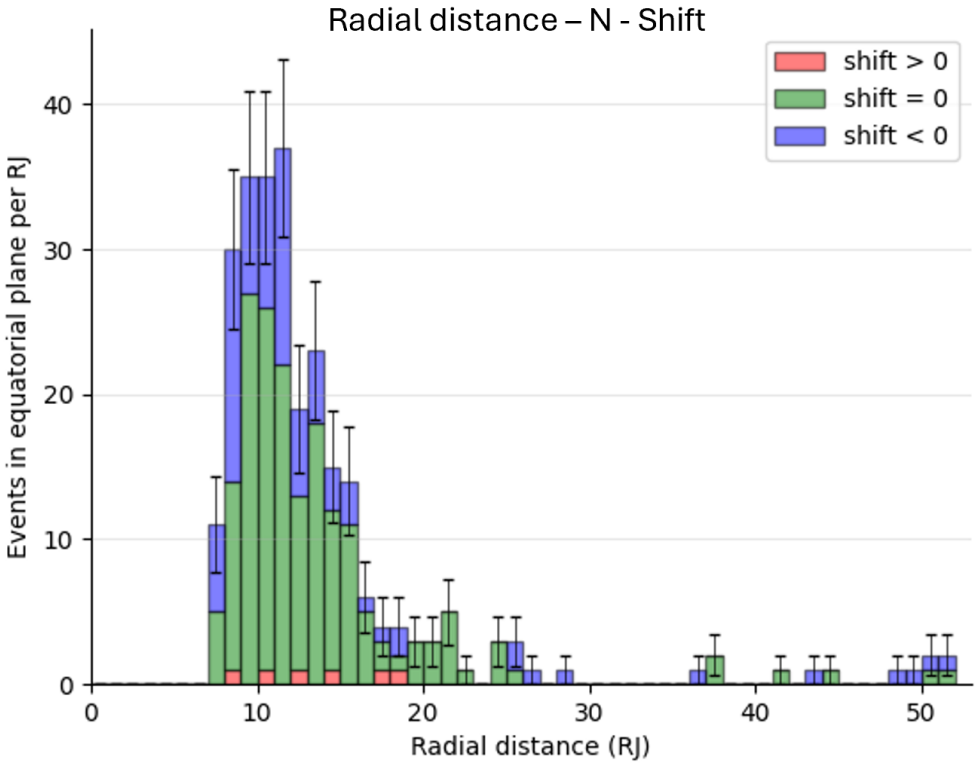

Figure 4.13 Distributions of structures detected in the Northern Hemisphere, magnetically mapped in the equatorial plane using the JRM33 magnetic field model, as a function of radial distance. The histogram contains a combination of three different shifts : no shift (green), negative shift (blue) and positive shift (red), Bin width is 3 hours LT. The error bars represent the statistical uncertainty on the number of events in each bin, calculated as the square root of the event counts, following the Poisson distribution.

In the Southern Hemisphere, the higher concentration of detection is located between 9 RJ and 19 RJ. The highest concentration of structure with no shift occurs between

11 RJ and 14 RJ, while for structures exhibiting a negative shift, this range is reduced to 13 RJ.

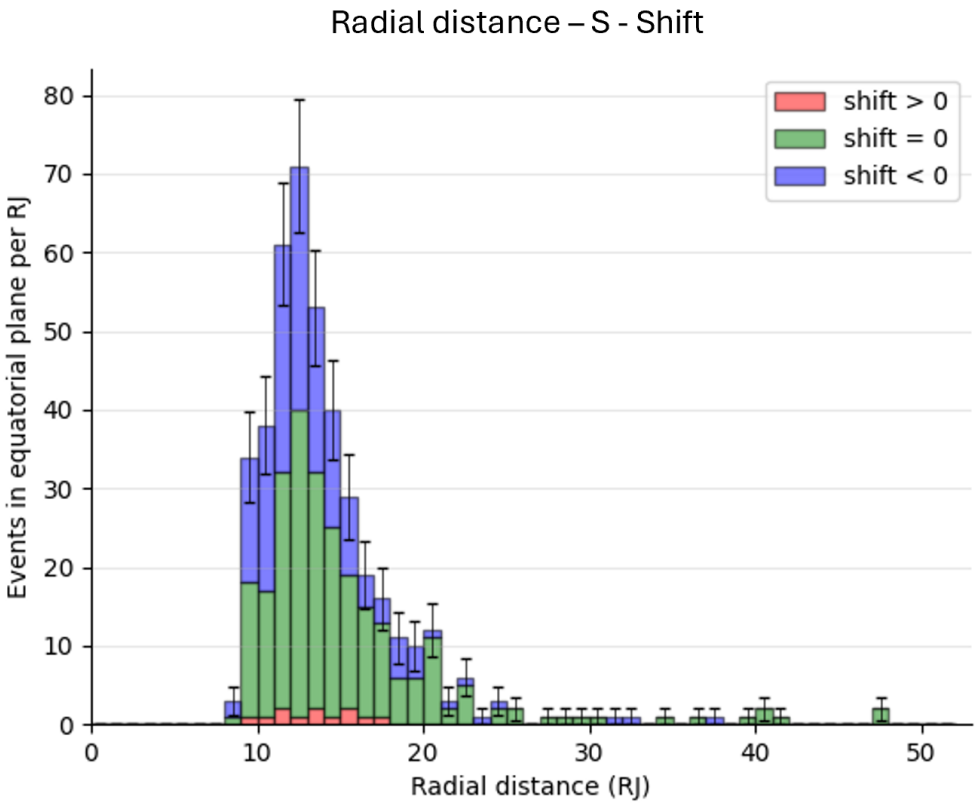

Figure 4.14 Distributions of structures detected in the Southern Hemisphere, magnetically mapped in the equatorial plane using the JRM33 magnetic field model, as a function of radial distance. The histogram contains a combination of three different shifts : no shift (green), negative shift (blue) and positive shift (red), Bin width is 3 hours LT. The error bars represent the statistical uncertainty on the number of events in each bin, calculated as the square root of the event counts, following the Poisson distribution.

Chapter 5

Discussions

This chapter discusses the results obtained in order to highlight their scientific significance and practical implications. First, the Problems Encountered and Solutions Provided section presents the difficulties encountered during the study and the strategies implemented to overcome them. Second, the Interpretation section provides an analysis of the trends observed, examining in particular positive shifts and geographical and temporal variations.

5.1 Problems encountered and solutions found

The detection step highlights the detected structures with a circle around each one. As can be seen from the Figure 5.1, sometimes two structures are located in the same circle. In this case, the center of the circle lies just between the two structures that could have been detected separately. As the center will be used to draw the arc on which the intensity will be taken to construct the light curve, the latter will not be relative to one of these structures. Indeed, the arc passes right between the 2 structures. To ensure that the line passes through a blob and not beside it, a window is created around the center of the detected structure. This window is drawn on a map created by adding several ribbons taken successively with a time interval of less than 5 minutes. This window is a square whose sides are twice the size of the detected structure plus 1. This addition ensures an odd number of pixels and therefore a central pixel in the window. Once the window has been constructed, the coordinates of the maximum intensity are saved and converted back into latitude and longitude coordinates relative to the starting file.

Initially, the code was designed to independently calculate the intensity based on the longitude of a specific structure for a given perijove. This approach was intended to ensure that the code functioned properly without requiring excessive computing time during this step. Once it worked, the code was expanded to calculate the intensity for all structures detected within a specific perijove. At that point, the calculation time increased significantly, exceeding one hour and thirty minutes and errors still persisted. To avoid further time wastage, the script was reorganized into

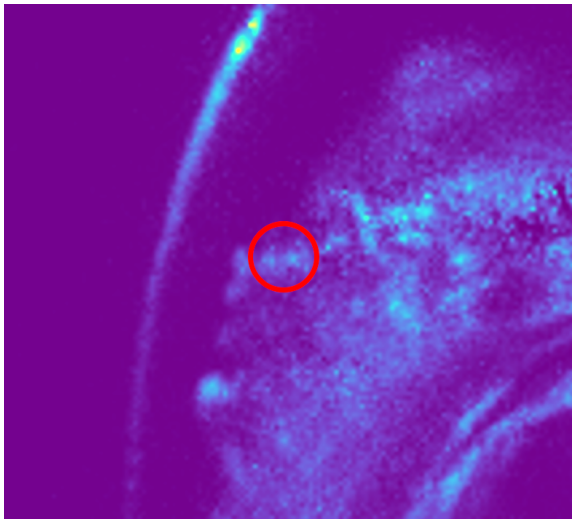

Figure 5.1 Zoom on the polar projection of Perijove 19 in the Northern Hemisphere. This image highlights a region where two distinct auroral structures are located along the same detection circle (red circle). This indicates that both features lie at approximately the same angular distance from the center of the projection (i.e., Jupiter's magnetic pole in this frame), and were therefore sampled simultaneously by the same circular detection profile.

three parts. This restructuring allows for quicker debugging; if one part encounters an issue, the time lost is much shorter compared to computing everything at once. The first part of the script extracts the names of the strips that provide more than 90% coverage for each structure. The second part constructs intensity curves as a function of the longitude, while the final part generates statistical distributions.

Several initialization problems were encountered, but they were resolved relatively quickly after the code was divided into several parts. In addition to these small issues, the code used to trace the magnetic field line passing through a specific point employed a different longitude convention than the one used in this study. This discrepancy was identified by tracing the field line associated with the footprint of Io, which is well known. The radial distance of Io, which is the distance between the point where the magnetic field line intersects the equatorial plane and the center of Jupiter, is 5.9 Rj (Khurana et al. 2004). However, when the longitude is applied as it is in plotting the magnetic field line, the measured radial distance reaches a different value of $\sim$ 17 Rj (for perijove 18 in the Northern Hemisphere). This model utilizes a longitude convention where angles are measured in the opposite direction (toward the west), starting from an origin at 0°. Therefore, to convert the longitudes provided by the detection code, expressed within the range of [0°, 360°] and measured clockwise toward the east, it is necessary to subtract the longitude from 360° to align with the correct system for the 'jrm33' model.

During the implementation of the method for tracing circular arcs, the initially planned approach consisted of directly generating an arc whose size corresponded to ten times the radius of the considered structure. The arc was constructed in the equatorial plane, then translated to the coordinates of the structure's center so that the midpoint of the arc coincided with that center. To achieve this, a first method

was tested: tracing the arc between the angles P - $\theta/2$ and P + $\theta/2$, where P is the angle determined from the x,y coordinates of the point on the magnetic field line closest to the equatorial plane, and θ the angular aperture corresponding to ten times its radius. However, after translation and conversion to latitude and longitude, this approach generated only a single point, not a curve. Other attempts were made by adjusting the parametric generation of the arc, but these resulted in either a single point or a poorly sized curve, often much too large. Finally, an alternative solution was adopted: an arc of arbitrarily large size was generated in the plane closest to the equatorial plane. It was then translated to the correct location according to the Cartesian coordinates of the structure's center. Once properly positioned, the arc was resized to reach the desired size, namely ten times the radius of the structure, while maintaining a regular and controlled distribution of points along the arc.

Another issue encountered during the analysis involved the generation of color ratio intensity as a function of longitude. During the computation of the color ratio intensity, the intensity values were initially extracted along a defined curve from two different maps: one constructed based on detection in the wavelength range 155-162 nm and the other based on the detection in the wavelength range 125-130 nm. These maps represent the same physical region, and the curve used for analysis was identical in terms of size, orientation, and location on both. The color ratio was defined as the point-by-point division of the intensity from the H_2Ly image by the intensity from the H_2We image. However, the resulting ratio curve turned out to be surprisingly constant. Moreover, the intensity values retrieved from the H_2We image were unexpectedly high,on the same order of magnitude as those from the H_2Ly image, despite the known fact that H_2We image should have significantly lower intensities. This inconsistency raised questions about the accuracy of the extracted intensity values. A plausible explanation for this anomaly lies in the polar projection (polar view) process applied to the maps. It appears that during the re-projection, the intensity values might have been rescaled or normalized, leading to distorted values that no longer represent the actual detected emission but rather a visually optimized output for display purposes. As a result, using these polar view images for quantitative analysis introduced a significant bias. To address this issue, instead of extracting data from the re-projected images, the raw intensity values are extracted from the original data files (with a resolution of 1800 $\times$ 3600). This method ensures that we are working with the true measured intensities, preserving the physical meaning of the data and allowing for a more accurate and reliable calculation of the intensity ratio.

During the analysis of the shifts between the brightness peaks and the color ratio peaks, it was found that some shifts were not associated with the correct peak. Specifically, the shifts were initially calculated by subtracting the maximum intensity in brightness from the maximum intensity in the color ratio. However, in some cases, the maximum intensity did not correspond to the relevant peak of interest, as shown in the figure, which led to inaccurate shift values. To address this issue, a more detailed analysis was performed. Each curve was manually examined to verify whether the calculated shifts indeed corresponded to the correct peaks.

5.2 Interpretations

This section offers an interpretation of the results obtained, highlighting the trends observed and the spatial relationships identified. The aim is to understand not only the significance of the variations noted, but also the potential mechanisms that could explain them.

The analysis will begin with an examination of positive shifts, before moving on to a more comprehensive interpretation of the variations, particularly in terms of spatial distribution and contrasts observed between the north and south.

5.2.1 Interpretations of the positive shifts observed in this study

The aim of this work was to demonstrate that the observed positive shifts were linked to the method used for assembling the maps. By using the mean number of events per 45° longitude step, it is possible to calculate the percentage of positive shifts occurring in the Northern and Southern Hemispheres. In the PhD thesis carried out by Maïté Dumont, these percentages were found to be 14.25 % for the Northern Hemisphere and 13.30 % for the Southern Hemisphere (Dumont 2023). In the present study, these values are lower : 6.5 % and 5.1 % for the Northern and Southern Hemispheres respectively. Given these results, it appears that some of the positive shifts observed in Maïté Dumont's thesis may indeed be attributed to the method used to construct the maps.

A manual verification was performed because, when defining the shift, the python code calculates the difference in longitude between the brightness maximum and the color ratio maximum. However, in some cases, two structures are located close to each other, and the resulting shift corresponds to the brightness maximum of one structure minus the color ratio maximum of another structure. Figure 5.2 illustrates this situation: the color ratio maximum appears at a longitude of 24°, which corresponds to the end of the curve from which the intensities were extracted. The color ratio peak associated with the structure of interest is actually around 19.5°, resulting in a shift near zero (between –0.9° and 0.9°), contrary to the negative shift reported by the code.

Despite performing manual verification and applying the intensity cutoff to ensure the accuracy of peak assignments, positive shifts still persisted, which, according to Maïté Dumont's hypothesis, should not occur (Dumont 2023). To further clarify these remaining positive shifts, RGB maps were generated to more accurately determine their true values, especially since the corresponding curves appeared blurred and ambiguous.

As previously explained, a yellow structure on the RGB maps indicates that the two peaks are located at the same longitude. In contrast, a red or green structure shows that the peaks are not aligned in longitude.

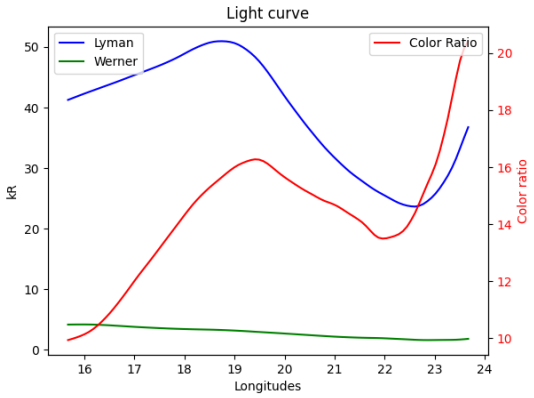

Figure 5.2 Illustration of a case where the computed shift is affected by the proximity of another structure. The color ratio maximum appears at 24° longitude (end of the intensity curve), whereas the peak associated with the structure of interest is around 19.5°, resulting in a near-zero shift (–0.9° to 0.9°) instead of the negative shift reported by the code.

For reference, one structure with coincident peaks (zero shift) and another structure with non-coincident peaks (negative shift) were selected.The RGB maps of the structure with no shift and with a negative shift are shown in Figure 5.3, on the left and right panels, respectively, where the structure of interest is circled in green. By comparing the RGB maps of structures with blurred curves to these two reference cases, it is possible to identify their shift as either zero, negative or positive. In addition to these RGB maps, the maps and curves from which the intensities are extracted, as well as the maps produced by Bertrand Bonfond, showing brightness and color ratio maps of Jupiter's auroras for each hemisphere are also used. A total of 18 structures with a positive shift were detected.

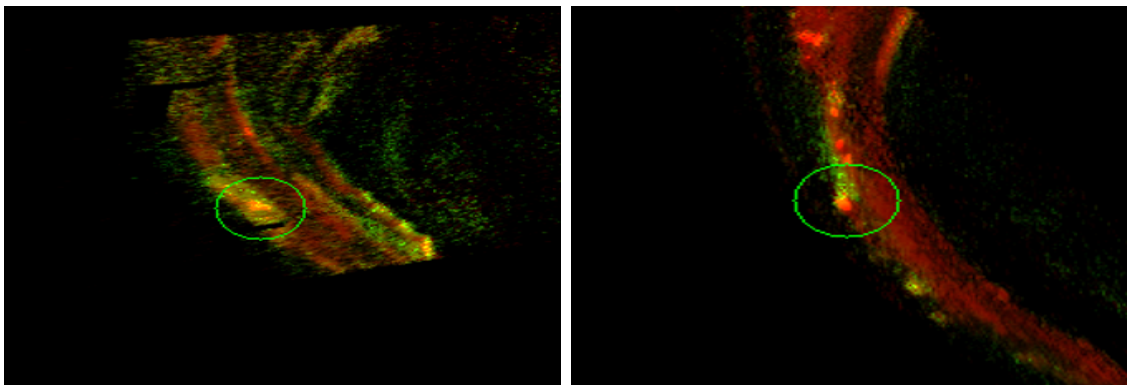

Figure 5.3 RGB maps of the structure with no shift (left panel) and with a negative shift (right panel). The maps have been processed with filters to maximize brightness and exposure while minimizing contrast. The region of interest is highlighted and shown with a zoom to clearly visualize the structure.

Among all the positive shifts identified, six show values located just beyond the upper limit of the interval considered as no shift (-0.9 to 0.9). These borderline cases indicate a small positive displacement, but one that is still sufficient to fall

outside the defined tolerance zone.

The other structures do not fit into the two hypotheses described above. Three of these structures are located in regions where the color ratio is relatively low (∼4 CR). These areas are fairly uniform, so no distinct peak in the color ratio could be reliably detected. A more complex case was observed where two green spots appear, one upstream and one downstream of the yellowish spot (Figure 5.4). The remaining structures were more complicated cases from which no clear interpretation could be drawn.

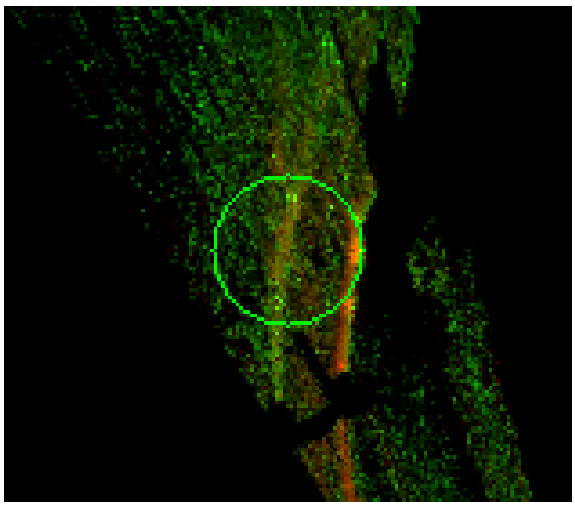

Figure 5.4 Example of a complex case showing two green spots (color ratio channel) located upstream and downstream of the yellowish spot (brightness channel), making the interpretation uncertain

Overall, the analysis revealed that while some positive shifts could be explained by methodological artifacts or borderline cases, others remained ambiguous due to low contrast or complex spatial configurations, preventing a definitive interpretation. The reduced number of positive shifts identified in this study compared to Dr. Maïté's findings indicates that the approach employed by Maïté Dumont may have introduced a greater proportion of false positives(Dumont 2023).

5.2.2 Statistical distribution of the detected structures

The small-scale structures in Jupiter's outer auroral emission are detected in much greater numbers and appear to be distributed over all longitudes and local times. In contrast, the large-scale structures are distributed more irregularly. While they may be present across the full range of longitudes and local times, certain regions contain only one or two such features. In this study, the distributions of small and large structures were examined separately for each hemisphere. A useful next step would be to combine both hemispheres into a single histogram, allowing for a direct comparison of their occurrence rates and distribution patterns. Such an approach could reveal asymmetries or similarities that are not apparent when analyzing the hemispheres independently. This combined analysis could also help to identify global

trends and improve our understanding of the processes responsible for generating small- and large-scale structures in Jupiter's outer auroral emission.

While the Northern Hemisphere exhibits significant inhomogeneities in the distribution of detected structures, the Southern Hemisphere presents a comparatively homogeneous pattern. A potential explanation for the observed inhomogeneous distribution in the Northern Hemisphere is linked to the intensity of the surface magnetic field. Jupiter's magnetic field exhibits an asymmetry between the hemispheres (Moore et al. 2018). In the northern hemisphere, the field is strongly non-dipolar. This non-dipolar structure creates localized anomalies and irregularities, leading to significant spatial variations in field strength and thus a highly heterogeneous magnetic field. In contrast, the southern hemisphere is predominantly dipolar, which results in a more uniform and homogeneous field. This difference in field morphology may help explain why the distribution of detected events is more uniform in the southern hemisphere, whereas the heterogeneous, non-dipolar field in the north could lead to a more uneven distribution.

In the Northern Hemisphere, the results show a low number of structure detections between 0° and 45° System III longitude, which could be attributed to an anomaly in the surface magnetic field. Grodent et al. (2008) sought to develop a surface magnetic field model capable of reproducing the HST observations of Io's footprint. To achieve this, they introduced a magnetic anomaly characterized by a localized weakening of the surface field within the so-called kink sector (System III longitudes 80°–150°). In addition, they incorporated a tilted dipolar component centered at 64° latitude and 107° longitude. The resulting surface magnetic field exhibits a pronounced reduction in intensity between 0° and 45° longitude. Depending on the electron acceleration mechanism, such a weakened field may reduce the efficiency of electron precipitation into the atmosphere (e.g.electron acceleration via Alfvén waves Hess et al. 2009), thereby leading to diminished auroral emissions within this longitudinal range, or increase the precipitating electron flux via a decrease of the altitude of the mirror point.

In the northern hemisphere, the results show a lower number of detections around 180° longitude. As shown by Connerney et al. (2018), at these longitudes the magnetic field reaches its maximum, around 20 Gauss, whereas in other regions it can drop below 2 Gauss. A possible explanation for this reduced detection rate is that the magnetic field is so strong that the external emission lies directly against the main emission. During mapping, the external emission at these longitudes could be included within the mask of the main emission, meaning that the external emissions may be effectively obscured by the main emission mask.

In the Southern Hemisphere, the results show an increase in the number of structures between 12:00 and 03:00 LT, while in the Northern Hemisphere the increase begins later, around 15:00 LT, and then decreases to reach a minimum between 06:00 and 09:00 LT. The increase observed could be explained by an asymmetric distribution of plasma injections. A study conducted by Dumont et al. (2014) showed that auroral signatures associated with plasma injections in Jupiter's magnetosphere are present at all System III longitudes, but their frequency and intensity can vary depending on longitude and local time. It is therefore possible that, during this period, conditions

favored a higher occurrence of these injections. It is also possible that injections were more intense in this region and weaker at other times, with the weaker injections falling below the intensity threshold used in this analysis. Plasma injections can propagate to large radial distances depending on the magnetospheric dynamics. Auroral structures observed at these radial distances may result from these injections. Therefore, the increased concentration of auroral structures observed between 7 and 16 RJ in the Northern Hemisphere and between 9 and 19 RJ in the Southern Hemisphere could be directly linked to the dynamics of plasma injections in these regions.

One possible source of these plasma injections is dawn storm activity. Juno-UVS observations reveal that dawn storms are a sequence of events lasting roughly 5 to 10 hours (Bonfond et al. 2021). They begin with the sudden appearance of transient spots in the premidnight sector. Two to three hours later, the midnight portion of the main auroral emission brightens, often forming a series of regularly spaced bead-like structures. As the event progresses, the brightened arc extends in longitude, gradually corotates with the planet, and shifts toward the dawn sector. The arc may then bifurcate, with one branch moving poleward. The space between the arcs fills in over time, and the structures broaden in latitude. Eventually, the overall emission dims, leaving the equatorward part of the dawn storm as a patch of emission that could be associated with plasma injection signatures, suggesting a possible link between dawn storms and some of these signatures. It is important to note that the disturbances generated by dawn storms are not confined to the location where the storm initially appears. One possible hypothesis is that, because dawn storms occur in the main auroral emission, they are initially hidden from direct detection in the outer emission. In this scenario, observations in the outer auroral regions would capture the storms only after they have propagated, rather than at their origin in the dawn sector of the main emission. This could potentially explain the observed increase in the number of detections after 12:00 LT.

Chapter 6

Conclusion

This study aimed to statistically analyze the auroral signatures associated with particle injections in Jupiter's magnetosphere, with a particular focus on the longitudinal shifts observed between brightness peaks and color ratio peaks. To this end, the detected auroral structures were analyzed based on their size, System III longitude, and local time, in both hemispheres. This approach allowed highlighting the distribution of different types of shifts, especially positive shifts, in order to better understand their origin and to test the hypothesis that these shifts might be related to map construction methods.

The results reveal clear hemispheric asymmetries in Jupiter's auroral dynamics. The northern hemisphere shows inhomogeneous distributions of detected structures, likely related to the strongly non-dipolar character of the magnetic field compared to the more dipolar southern field. A deficit of detections around 180° longitude in the north may be explained by overlap between the main and outer emissions, with the latter hidden by the mask applied to the main emission. In this hemisphere, the lower number of detections between 0° and 45° in longitude could be due to a magnetic anomaly, which might reduce the efficiency of electron precipitation in the atmosphere. In the southern hemisphere, an increase in the number of detected structures is observed between 12:00 and 03:00 LT, while in the northern hemisphere this increase begins later, around 15:00 -18:00 LT, reaches a maximum between 18:00 and 21:00 LT, and then decreases to a minimum between 06:00 and 09:00 LT. These variations may reflect enhanced injection activity, possibly linked to dawn storms originating on the dawn side of the main emission.

Additionally, the observed longitudinal shifts between brightness and color ratio peaks can be interpreted in terms of the differential drift of particles injected from the middle to the inner magnetosphere. Cases with no shift indicate young injection, for which particle populations still remain together, so the brightness and color ratio peaks coincide. In contrast, negative shifts occur when higher-energy particles have already begun their drift relative to lower-energy particles, producing the observed offset downstream of the brightness peak. This provides further evidence that these auroral features are closely tied to radial plasma transport and energy-dependent particle dynamics within Jupiter's magnetosphere.

Compared to previous studies, the reduced occurrence of positive shifts observed here strengthens the conclusion that earlier results were influenced by methodological biases. Overall, these findings highlight the importance of both magnetic field asymmetries and dynamic plasma processes in shaping auroral variability.

Bibliography

Abel, Bob and Richard M Thorne (2003). "Relativistic charged particle precipitation into Jupiter's sub-auroral atmosphere". In: *Icarus* 166.2, pp. 311–319.

Alfvén, Hannes (1942). "Existence of electromagnetic-hydrodynamic waves". In: *Nature* 150.3805, pp. 405–406.

Atreya, SK et al. (1999). "A comparison of the atmospheres of Jupiter and Saturn: deep atmospheric composition, cloud structure, vertical mixing, and origin". In: *Planetary and Space Science* 47.10-11, pp. 1243–1262.

Atreya, SK et al. (2003). "Composition and origin of the atmosphere of Jupiter—an update, and implications for the extrasolar giant planets". In: *Planetary and Space Science* 51.2, pp. 105–112.

Benmahi, Bilal et al. (2024). "Auroral 3D structure retrieval from the Juno/UVS data". In: *Astronomy & Astrophysics* 691, A91.

Bhardwaj, Anil and G Randall Gladstone (2000). "Auroral emissions of the giant planets". In: *Reviews of Geophysics* 38.3, pp. 295–353.

Bolton, Scott J et al. (2015). "Jupiter's magnetosphere: Plasma sources and transport". In: *Space Science Reviews* 192, pp. 209–236.

Bolton, Scott J et al. (2017). "The juno mission". In: *Space Science Reviews* 213, pp. 5–37.

Bonfond, Bertrand and Ali Sulaiman (2024). "Alfvén Waves Related to Moon–Magnetosphere Interactions". In: *Alfvén Waves Across Heliophysics: Progress, Challenges, and Opportunities*, pp. 139–161.

Bonfond, Bertrand, Zhonghua Yao, and Denis Grodent (2020). "Six pieces of evidence against the corotation enforcement theory to explain the main aurora at Jupiter". In: *Journal of Geophysical Research: Space Physics* 125.11, e2020JA028152.

Bonfond, Bertrand et al. (2013). "The multiple spots of the Ganymede auroral footprint". In: *Geophysical Research Letters* 40.19, pp. 4977–4981.

Bonfond, Bertrand et al. (2017a). "Morphology of the UV aurorae Jupiter during Juno's first perijove observations". In: *Geophysical Research Letters* 44.10, pp. 4463–4471.

Bonfond, Bertrand et al. (2017b). "The tails of the satellite auroral footprints at Jupiter". In: *Journal of Geophysical Research: Space Physics* 122.8, pp. 7985–7996.

Bonfond, Bertrand et al. (2021). "Are dawn storms Jupiter's auroral substorms?" In: *AGU advances* 2.1, e2020AV000275.

Broadfoot, AL et al. (1981). "Overview of the Voyager ultraviolet spectrometry results through Jupiter encounter". In: *Journal of Geophysical Research: Space Physics* 86.A10, pp. 8259–8284.

Clarke, John T et al. (2004). "Jupiter's aurora". In: *Jupiter: The planet, satellites and magnetosphere* 1, pp. 639–670.

Connerney, JEP et al. (2018). "A new model of Jupiter's magnetic field from Juno's first nine orbits". In: *Geophysical Research Letters* 45.6, pp. 2590–2596.

Connerney, JEP et al. (2022). "A new model of Jupiter's magnetic field at the completion of Juno's prime mission". In: *Journal of Geophysical Research: Planets* 127.2, e2021JE007055.

Cowley, SWH and EJ Bunce (2001). "Origin of the main auroral oval in Jupiter's coupled magnetosphere–ionosphere system". In: *Planetary and Space Science* 49.10-11, pp. 1067–1088.

Dumont, Maıté (2023). *Ultraviolet Auroral Emissions Associated With Plasma Injections in Jupiter's Magnetosphere*. Universite de Liege (Belgium).

Dumont, Maıté et al. (2014). "Jupiter's equatorward auroral features: Possible signatures of magnetospheric injections". In: *Journal of Geophysical Research: Space Physics* 119.12, pp. 10–068.

Encrenaz, Thérèse (1999). "The planet Jupiter". In: *The Astronomy and Astrophysics Review* 9.3, pp. 171–219.

Ganushkina, N Yu, MW Liemohn, and Stepan Dubyagin (2018). "Current systems in the Earth's magnetosphere". In: *Reviews of Geophysics* 56.2, pp. 309–332.

Gérard, J-C et al. (2013). "Hubble observations of Jupiter's north–south conjugate ultraviolet aurora". In: *Icarus* 226.2, pp. 1559–1567.

Gérard, J-C et al. (2014). "Mapping the electron energy in Jupiter's aurora: Hubble spectral observations". In: *Journal of Geophysical Research: Space Physics* 119.11, pp. 9072–9088.

Gérard, J-C et al. (2016). "The color ratio-intensity relation in the Jovian aurora: Hubble observations of auroral components". In: *Planetary and Space Science* 131, pp. 14–23.

Gladstone, G Randall et al. (2017a). "The ultraviolet spectrograph on NASA's Juno mission". In: *Space Science Reviews* 213, pp. 447–473.

Gladstone, GR et al. (2017b). "Juno-UVS approach observations of Jupiter's auroras". In: *Geophysical Research Letters* 44.15, pp. 7668–7675.

Greathouse, Thomas et al. (2021). "Local time dependence of Jupiter's polar auroral emissions observed by Juno UVS". In: *Journal of Geophysical Research: Planets* 126.12, e2021JE006954.

Grodent, Denis (2015). "A brief review of ultraviolet auroral emissions on giant planets". In: *Space Science Reviews* 187, pp. 23–50.

Grodent, Denis et al. (2003). "Jupiter's polar auroral emissions". In: *Journal of Geophysical Research: Space Physics* 108.A10.

Grodent, Denis et al. (2006). "Europa's FUV auroral tail on Jupiter". In: *Geophysical Research Letters* 33.6.

Grodent, Denis et al. (2008). "Auroral evidence of a localized magnetic anomaly in Jupiter's northern hemisphere". In: *Journal of Geophysical Research: Space Physics* 113.A9.

Grodent, Denis et al. (2018). "Jupiter's aurora observed with HST during Juno orbits 3 to 7". In: *Journal of Geophysical Research: Space Physics* 123.5, pp. 3299–3319.

Groulard, Antoine et al. (2022). "Analysis of the dawn-dusk asymmetry in Jupiter's main auroral emission using Juno-UVS". In.

Head, LA et al. (2025). "Jupiter's ultraviolet auroral bridge: the influence of the solar wind on polar auroral morphology". In: *arXiv preprint arXiv:2504.07222*.

Head, Linus Alexander et al. (2024). "Effect of magnetospheric conditions on the morphology of Jupiter's ultraviolet main auroral emission as observed by Juno-UVS". In: *Astronomy & Astrophysics* 688, A205.

Helmenstine, Anne (Mar. 2023). *Aurora Colors Explained - Southern and Northern Lights*. en-US. Accessed on 06-03-2025. URL: `https://sciencenotes.org/aurora-colors-explained-southern-and-northern-lights/` (visited on 03/06/2025).

Hess, S et al. (2009). "Electric potential jumps in the Io-Jupiter flux tube". In: *Planetary and Space Science* 57.1, pp. 23–33.

Hill, TW (2001). "The Jovian auroral oval". In: *Journal of Geophysical Research: Space Physics* 106.A5, pp. 8101–8107.

Hill, TW and VM Vasyliūnas (2002). "Jovian auroral signature of Io's corotational wake". In: *Journal of Geophysical Research: Space Physics* 107.A12, SMP–27.

Hue, V et al. (2022). "A comprehensive set of Juno in situ and remote sensing observations of the Ganymede auroral footprint". In: *Geophysical Research Letters* 49.7, e2021GL096994.

Hue, Vincent et al. (2019). "In-flight characterization and calibration of the Juno-ultraviolet spectrograph (Juno-UVS)". In: *The Astronomical Journal* 157.2, p. 90.

Ingersoll, Andrew P et al. (1998). "Imaging Jupiter's aurora at visible wavelengths". In: *Icarus* 135.1, pp. 251–264.

Ingersoll, Andrew P et al. (n.d.). "Dynamics of Jupiter's Atmosphere". en. In: ().

Irwin, PGJ et al. (2001). "The origin of belt/zone contrasts in the atmosphere of Jupiter and their correlation with 5-μm opacity". In: *Icarus* 149.2, pp. 397–415.

Jacobsen, S et al. (2007). "Io's nonlinear MHD-wave field in the heterogeneous Jovian magnetosphere". In: *Geophysical research letters* 34.10.

Khurana, Krishan K (2001). "Influence of solar wind on Jupiter's magnetosphere deduced from currents in the equatorial plane". In: *Journal of Geophysical Research: Space Physics* 106.A11, pp. 25999–26016.

Khurana, Krishan K et al. (2004). "The configuration of Jupiter's magnetosphere". In: *Jupiter. The planet, satellites and magnetosphere* 1, pp. 593–616.

Kivelson, Margaret Galland (2005). "The current systems of the Jovian magnetosphere and ionosphere and predictions for Saturn". In: *Space Science Reviews* 116.1, pp. 299–318.

Kivelson, Margaret Galland and Fran Bagenal (2014). "Planetary magnetospheres". In: *Encyclopedia of the solar system*. Elsevier, pp. 137–157.

Lysak, RL (2023). "Kinetic Alfvén waves and auroral particle acceleration: A review". In: *Reviews of Modern Plasma Physics* 7.1, p. 6.

Mauk, BH et al. (2002). "Transient aurora on Jupiter from injections of magnetospheric electrons". In: *Nature* 415.6875, pp. 1003–1005.

Moore, Kimberly M et al. (2018). "A complex dynamo inferred from the hemispheric dichotomy of Jupiter's magnetic field". In: *Nature* 561.7721, pp. 76–78.

Moses, Julianne I et al. (2004). "The stratosphere of Jupiter". In: *Jupiter: Planet, Satellites and Magnetosphere*, pp. 129–157.

Pierrard, Viviane (2009). "Kinetic models for the exospheres of Jupiter and Saturn". In: *Planetary and Space Science* 57.11, pp. 1260–1267.

Planetary Satellite Discovery Circumstances (2025). URL: https://ssd.jpl.nasa.gov/sats/discovery.html (visited on 07/26/2025).

Radioti, Aikaterini et al. (2008). "Discontinuity in Jupiter's main auroral oval". In: *Journal of Geophysical Research: Space Physics* 113.A1.

Radioti, Aikaterini et al. (2009). "Equatorward diffuse auroral emissions at Jupiter: Simultaneous HST and Galileo observations". In: *Geophysical Research Letters* 36.7.

Saha, Kshudiram and Kshudiram Saha (2008). "The Earth's Atmosphere–Its Origin, Composition and Properties". In: *The Earth's Atmosphere: Its Physics and Dynamics*, pp. 9–26.

Saur, Joachim, Annick Pouquet, and William H Matthaeus (2003). "An acceleration mechanism for the generation of the main auroral oval on Jupiter". In: *Geophysical Research Letters* 30.5.

Saur, Joachim et al. (2018). "Wave-particle interaction of Alfvén waves in Jupiter's magnetosphere: Auroral and magnetospheric particle acceleration". In: *Journal of Geophysical Research: Space Physics* 123.11, pp. 9560–9573.

Stevenson, DJ (1983). "Planetary magnetic fields". In: *Reports on Progress in Physics* 46.5, p. 555.

Tomás, Ana Teresa et al. (2004). "Energetic electrons in the inner part of the Jovian magnetosphere and their relation to auroral emissions". In: *Journal of Geophysical Research: Space Physics* 109.A6.

Tsurutani, Bruce T et al. (1997). "Plasma wave characteristics of the Jovian magnetopause boundary layer: Relationship to the Jovian aurora?" In: *Journal of Geophysical Research: Space Physics* 102.A3, pp. 4751–4764.

Vasavada, Ashwin R and Adam P Showman (2005). "Jovian atmospheric dynamics: An update after Galileo and Cassini". In: *Reports on Progress in Physics* 68.8, p. 1935.

Waite Jr, JH et al. (2000). "Multispectral observations of Jupiter's aurora". In: *Advances in Space Research* 26.10, pp. 1453–1475.

Wilson, RJ et al. (2023). "Internal and external Jovian magnetic fields: Community code to serve the magnetospheres of the outer planets community". In: *Space Science Reviews* 219.1, p. 15.

Yao, ZH et al. (2022). "On the relation between auroral morphologies and compression conditions of Jupiter's magnetopause: Observations from Juno and the Hubble Space Telescope". In: *Journal of Geophysical Research: Space Physics* 127.10, e2021JA029894.

Yelle, Roger V and Steven Miller (2004). "Jupiter's thermosphere and ionosphere". In: *Jupiter: The planet, satellites and magnetosphere* 1, pp. 185–218.

Yung, Yuk L et al. (1982). "H2 fluorescence spectrum from 1200 to 1700 A by electron impact-Laboratory study and application to Jovian aurora". In: *Astrophysical Journal, Part 2-Letters to the Editor, vol. 254, Mar. 15, 1982, p. L65-L69.* 254, pp. L65–L69.